2018-10

Investigation of effective stress intensity factors during overload fatigue cycles using photoelastic and DIC techniques

Vasco-Olmo, JM

10.1016/j.tafmec.2018.07.011
Theoretical and Applied Fracture Mechanics
Elsevier

Investigation of effective stress intensity factors during overload fatigue cycles using photoelastic and DIC techniques

J.M. Vasco-Olmo[1], Bing Yang[2], M.N. James[3, 4] and F.A. Díaz[1]

[1]Departamento de Ingeniería Mecánica y Minera, University of Jaén, Jaén, Spain

[2]State Key Laboratory of Traction Power, Southwest Jiaotong University, Chengdu, China

[3]School of Engineering, University of Plymouth, Plymouth, England

[4]Department of Mechanical Engineering, Nelson Mandela University, Port Elizabeth, South Africa

Abstract

This work uses DIC and photoelastic techniques to investigate the effect of single overload cycles applied during constant amplitude fatigue. Effective values of the range of stress intensity factor were calculated using the CJP model of crack tip stress and displacement fields, as this model considers both wake contact and compatibility-induced influences on the applied elastic field arising from the plastic enclave generated around a fatigue crack. Values of the effective stress intensity factor are related to the observed crack growth acceleration and retardation. In addition, the paper compares the CJP results with those obtained using a compliance-based method. The present work demonstrates the utility of the CJP model in characterising fatigue crack growth rates during variable amplitude loading. It is also possible with the CJP model, through changes in the coefficient values and hence, for the first time, to shed explicit light on the contributions made by different mechanisms to the shielding effects of an overload.

Keywords: crack tip fields, fatigue crack growth, overloads, plasticity-induced shielding, stress intensity factor.

Nomenclature:

A, B, C, E, F:	coefficients in the CJP model
f_σ:	material stress fringe value
G:	shear modulus
i:	square root of -1
j:	j^{th} collected data point
K_F:	stress intensity factor driving crack growth in the CJP model

K_I:	mode I stress intensity factor
K_R:	CJP stress intensity factor acting to retard crack growth
N:	fringe order
R:	ratio between the minimum and the maximum applied load in fatigue
r, θ:	polar coordinates around the crack tip
r_p:	monotonic plastic zone size according to Irwin estimate
T:	T-stress
t:	specimen thickness
u, v:	components of the displacement vector
E:	Young's modulus
ΔK_{eff}:	effective range of stress intensity factor
ΔK_{nom}:	nominal range of stress intensity factor
γ:	isoclinic angle
δ:	relative retardation in transmission photoelasticity
κ:	function of Poisson's ratio
v:	Poisson's ratio
σ_x, σ_y, σ_{xy}:	stress components in Cartesian coordinates

1. Introduction

The mechanisms driving fatigue crack growth have been of interest for many years, but despite considerable effort there are still some issues that remain either incompletely understood or controversial. Plasticity-induced crack shielding (or crack closure) is one such phenomenon, where there is no consensus on the conditions under which it occurs, its magnitude, the most appropriate measurement techniques(s) or the interpretation of its influence on fatigue phenomena [1]. Nonetheless, mean stress or stress ratio effects on fatigue crack growth rate data under constant amplitude loading can often be reduced to a narrow scatter band by invoking shielding mechanisms, e.g. [2], [3]. In the case of variable amplitude loading, however, which in the most simple case involves the application of a single spike overload, the mechanisms that underlie the temporary acceleration and retardation observed in fatigue crack growth rate remain uncertain. Shin and Hsu in a study of overload retardation in 304 stainless steel concluded that the major mechanism behind crack growth retardation was plasticity-induced closure [4]. Sadananda et al. [6], [7] proposed a two-parameter approach based on both ΔK and K_{max} concluding that the role of closure contributions to overload effects could be minor and that residual or internal stresses were important in understanding fatigue crack growth behaviour. Alderliesten [8] takes an even more radical approach, noting that the majority of crack propagation relationships are completely phenomenological and are not derived from physical principles. He suggests that the fatigue problem should be discussed from a physics perspective so that more appropriate crack growth rate equations can be formulated, other than those based on the stress intensity factor which has well-known similitude problems, including crack tip shielding issues. The problem of achieving better understanding of the physical mechanisms involved in fatigue crack grow this compounded by difficulties with precise quantification of crack tip shielding effects, since measurement techniques used for this are often based on indirect experimental measurements and/or may be complex and time-consuming to perform.

Hence the techniques for handling variable amplitude cyclic loading in life prediction have advanced little further since the formulation of the linear damage summation rule by Palmgren in 1924 and Miner in 1945 which has known shortcomings in respect of load sequence effects. In general, however, the application of a single spike overload during constant amplitude fatigue loading usually results in an overall crack growth rate retardation. Prior to the overload the crack tip plastic zone steadily increases in size as a function of crack length, while the application of the overload produces an

instantaneous increase in the size of the plastic zone at the crack tip and an associated transient increase in crack growth rate, usually followed by delayed retardation. Several authors have proposed that when an overload is applied there is an initial extension of the crack that is greater than that corresponding to constant amplitude loading, e.g. [4]. The subsequent retardation effect then occurs as the crack propagates through the enlarged plastic zone generated by the overload. The contribution to retardation arising from increased wake contact (closure) or from a residual stress influence of the enlarged plastic zone is still unclear and it is in this area that the present paper makes a contribution. It presents data for the effective range of stress intensity factor through single overload cycles and compares CJP model calculations of effective stress intensity factor with those obtained using traditional compliance-based techniques. The formulation of the terms in the CJP model of crack tip stresses allows, in principle, insight to be gained into the relative contribution to the effective stress intensity range from wake contact and from compatibility-induced residual stresses at the elastic-plastic boundary. It is then also possible to determine whether other influences are also involved in the observed changes to crack growth rate following an overload.

The development of optical full-field experimental techniques, such as transmission photoelasticity [9] and digital image correlation (DIC) [10], to characterise crack tip displacement, strain and stress offers significant potential for a better understanding of the mechanisms that both drive fatigue crack growth, and lead to shielding or retardation induced by crack propagation. Full-field techniques have also led to improved experimental determination of stress intensity factors (SIFs) from the analysis of strain, stress and displacement fields in the vicinity of the tip of a growing fatigue crack. Several different models have been proposed over the years to describe crack tip stress and displacement fields. The main models reported in the literature are based either on Westergaard's equations [11], Williams' expansion series [12] or Muskhelishvili complex potentials [13] and have been described in terms of both stress fields (e.g. using Westergaard [11], Williams [14] and Muskhelishvili [15]) and displacement fields (e.g. using Westergaard [11], Williams [16] and Muskhelishvili [17]).

Such models generally ignore any consequences of the plasticity induced by a growing fatigue crack and there is clearly scope for developing an improved model of crack tip stress fields that incorporates influences of the plasticity-induced shielding on a growing fatigue crack. These are likely to include crack wake contact and other residual

stress effects arising from the enlarged plastic zone contingent on the overload. In the formulation of such a model, it is desirable to avoid the analytical complexities of plastic deformation by focusing attention on the influence of the elastic stresses that would be induced at the elastic-plastic boundary by the plastically deformed enclave that surrounds a crack. Such a model has been proposed and developed by Christopher, James and Patterson [18] and co-workers, and is referred as the CJP model by its originators.

2. Progress in the development of the CJP model

The CJP model of crack tip fields [18] is based on Muskhelishvili's complex potentials [13]. It was specifically developed as an endeavour to obtain an elastic stress field model that explicitly captures the influences of an embedded region of plasticity surrounding a growing fatigue crack. This plastic enclave is therefore considered to shield the crack from the full influence of the elastic stress field that drives fatigue crack growth. The model further proposes that these plasticity-induced effects can be assessed through incorporation of the influence of interfacial stresses at the elastic-plastic boundary on the elastic stress field ahead of the crack tip.

Details of the model have been presented in other papers [18]–[21] and will not be repeated here. It is sufficient to note that the model used assumed distributions of elastic stresses induced at the elastic-plastic boundary via wake contact and compatibility requirements, and defines a set of modified elastic stress intensity factors [18] to characterise the crack tip field. These stress intensity factors reflect a combination of applied stress and any plasticity-induced elastic stresses that characterise crack tip shielding. These stresses are considered to arise from wake contact (crack closure) and from compatibility-induced elastic-plastic boundary stresses as Poisson's ratio is different in the plastic and elastic regions. Incorporation of a Mode II component of load into the CJP model [22] should also enable any influences of surface roughness-induced closure to be accounted for in the solution. The model therefore leads to a stress intensity factor that drives crack growth (called K_F which, in the absence of plasticity-induced shielding, is identical to K_I) and a retarding stress intensity factor (K_R) that includes both crack wake contact and the possibility of stresses induced through compatibility requirements at the elastic-plastic interface, and which have an effect on the elastic stress field ahead of the crack. It also calculates a value for the *T*-stress.

In its current state of development, the CJP model can be applied to crack tip stress or displacement fields and it has been independently shown that the model can give accurate values of the effective range of stress intensity factor [23]. Whilst it is true that the effective range of stress intensity factor can easily be obtained using certain full-field experimental techniques, e.g. thermoelastic stress analysis, the CJP model is unique in its ability to provide accurate values of the effective stress intensity range whilst also giving insights into the mechanisms underlying the plasticity-induced shielding phenomenon. This is possible because the relative contributions and influence that arise from *T*-stress, crack wake contact, compatibility-induced strains at the elastic-plastic interface or from fracture surface roughness can, in principle, be explored by independently varying the values of the various coefficients of the terms in the mathematical model (*A*, *B, C*, *E* and *F*) [22], and by examining their changes throughout overload cycles.

Until the 1990s, photoelasticity was the only experimental full-field technique that was widely available, and experimental fracture mechanics work using photoelasticity generally used specimens manufactured from brittle epoxy resins, that contained sharp notches to simulate cracks. Such brittle resin specimens were not suitable for growing fatigue cracks, and therefore photoelasticity was not employed to evaluate phenomena associated with fatigue crack growth, such as crack closure or crack tip shielding. However, work reported many years ago by James and Knott [24] showed that polycarbonate is a birefringent material that is sufficiently ductile to allow the study of fatigue crack growth and to show clear evidence of plasticity-induced shielding. In the original work by James et al. [25] that used polycarbonate CT specimens and phase-stepping photoelasticity to examine the growth of fatigue cracks and the role of crack closure, a more simple mathematical analysis was used that was intended to investigate whether values for a single-point wake contact force could be derived from a combination of full-field photoelasticity and an analytical model for crack tip stresses that incorporated wake contact forces. Transmission photoelasticity was employed to analyse the variation in wake contact forces through load cycles applied to 2 mm thick polycarbonate compact-tension (CT) specimens containing growing fatigue cracks. A random variation in wake contact pressure was recorded in this work, i.e. there was no clear relationship with the applied load variation, and this led the authors to subsequently propose that the complete plastic enclave around a fatigue crack acts to shield the crack from the influence of the applied stress field.

A more complex and advanced crack tip stress model was subsequently developed that included the applied stresses, an exponential decay in wake contact force behind the crack tip, compatibility-induced interfacial shear stresses at a notional elastic-plastic boundary and a *T*-stress. The interfacial shear stresses were primarily proposed to exist and act along the direction of crack growth, although there may also be a component acting through the thickness of the specimen (although this would be limited by the small specimen thickness used in work to date). This new model was above referred as the CJP model in reference [19]. Further work by Christopher et al. [21] investigated the mechanisms controlling the phenomenon of plasticity-induced shielding by using digital phase-stepping photoelasticity.

The advantage of photoelasticity is that the isochromatic fringe patterns show contours of difference in principal stress that can be directly compared with corresponding output from the CJP model of crack tip stresses. Several papers have presented such data and drawn conclusions regarding the influence of plasticity-induced shielding on the elastic stress field that drives crack growth [18], [25]–[26]. The experimental results demonstrated clear and sensible trends in the new stress intensity terms defined by the CJP model that appeared to reflect the operation of mechanisms believed to underlie the phenomenon of plasticity-induced shielding.

More recently, James et al. [19] extended the use of the CJP model to include a solution for the crack tip displacement fields that allowed the model to be applied to metallic specimens using DIC techniques. That paper was intended to explain clearly the thinking and development process behind this innovative meso-scale model for a multi-parameter characterisation of the elastic stress field around a crack contained within a plastic enclave. It analysed the optimum size and shape of the crack tip region used in the fitting process between theory and experiment, and compared errors in fitting the experimental fringe patterns to either a 2-term or 4-term Williams solution, or to the CJP model. Ancillary issues were also considered, including the repeatability of data between duplicate tests and whether the observed trends were sensitive to crack length or stress ratio. The authors concluded that the CJP model offered a meso-scale bridge between the plasticity-induced consequences of crack growth mechanisms and the continuum elastic stress field driving crack growth. Values of the new stress intensity parameters defined in the model behaved rationally in fatigue tests performed

on birefringent polycarbonate CT specimens, leading to effective values of K_{max} that were lower than the applied value and effective values of K_{min} that were higher than the applied value. The model therefore provides insight, at least to some extent, into the fundamental question of how fatigue crack growth, a phenomenon which explicitly derives from plastic deformation, can be accurately described by an elastically-derived parameter, i.e. the stress intensity factor, under conditions where there is a plasticity-induced loss of similitude.

A recently published paper [27] demonstrates that the CJP model provides an effective rationalisation of fatigue crack growth data across several geometries of Grade 2 titanium specimens and various stress ratio values, with the added advantage that the usual geometric compliance correction factors are not necessary in the calculation of the CJP stress intensity factors. Additionally, calibration curves were derived that related the parameters ΔA, ΔB and ΔD in the CJP stress intensity factors K_F and K_R to values of the standard ΔK. For the case of CT specimens linear relationships were found, while for double edge-notched tension (DENT) specimens the relationships for ΔA and ΔB were quadratic. The relationship between ΔD and ΔK for DENT specimens could be fitted with either a quadratic or a linear equation. The authors concluded that the CJP model of crack tip fields can simultaneously provide insight into the underlying mechanisms of plasticity-induced shielding and predict the effective driving force for fatigue crack growth, characterised by ΔK_{CJP} [27]. It therefore offers a powerful advantage in fatigue life prediction by explicitly incorporating plasticity-induced shielding forces and, through a modification to include Mode II loading, can potentially deal with roughness-induced closure [22].

Other recent work by some of the present authors [26], has evaluated the plasticity-induced crack shielding effect during fatigue crack growth using transmission photoelasticity [26] and DIC [28]. These papers compared four different crack tip stress field models (Westergaard, Williams, Muskhelishvili and CJP) and concluded, perhaps unsurprisingly, that the CJP model was the most suitable for the evaluation of fatigue crack shielding. The work in reference [26] used polycarbonate centre-cracked tension (CCT) specimens tested at several different stress ratios, and a retardation effect on fatigue crack growth rate due to shielding was observed for tests conducted at low values of stress ratio. Transmission photoelasticity used in conjunction with the CJP model has therefore been shown to be useful in the study of fatigue and fracture

problems in ductile birefringent materials [26], [29]. The predictions of shielding obtained using DIC have been compared with those obtained from notch-mouth compliance measurements using an extensometer [28]. Recently, it has been also demonstrated that the size and shape of the crack tip plastic zone can be accurately predicted by the CJP model [20].

Overload phenomena have attracted significant research attention over many years with little agreement on how to incorporate them into life prediction except via a linear damage summation process that does not account for load interaction effects on crack growth rate. Through its ability to simultaneously provide insight into the underlying mechanisms of plasticity-induced shielding and give the effective driving force for fatigue crack growth, characterised by ΔK_{CJP}, the CJP model is well suited to advancing understanding of how fatigue overloads affect crack growth rate. In this respect, work reported by Colombo et al [30] used the CJP model to study the change in the crack closure effect during and after an overload using a polycarbonate compact tension specimen. Their study concluded that plasticity-induced shielding had a substantial effect on fatigue crack growth rates as a consequence of (a) a stress field established ahead of the crack generated by the presence of the crack tip plastic zone and acting to oppose crack extension; and (b) an interfacial shear stress at the elastic–plastic boundary between the plastic zone in the crack wake and the surrounding elastic material. The direction of this shear field was seen to reverse during the fatigue cycle and to be much stronger when the crack was open and following an overload. DIC techniques have been used by other workers to evaluate the effect of overloads by measuring the relative displacements between pairs of points located behind the crack tip at each flank of the fracture [31], [32].

The present study uses the CJP model to quantify the effects of single fatigue overloads on the effective range of stress intensity factor. From consideration of the various coefficients in the CJP model and their changes during an overload, conclusions can be drawn regarding the parameters that may be influential in the growth rate transients that are associated with an overload cycle. The CJP model was fitted to experimental photoelastic isochromatic stress fringe patterns and DIC displacement fringe data. Work on the polycarbonate CT specimen used overload levels of 50%, 100% and 200%, while the work on aluminium CT specimens applied overloads of 100% and 125%. Values for the effective stress intensity factor range

obtained from the CJP model using DIC data were compared with the values obtained with a compliance-based technique, where crack opening displacement (COD) was recorded with an extensometer located at the notch mouth.

3. Experimental work

The experimental work used 2 mm thick compact tension (CT) specimens (geometry and dimensions as shown in Figure 1) manufactured from sheets of polycarbonate for the photoelastic experiments and from 2024-T3 aluminium alloy for DIC work. The mechanical properties (Young's modulus, yield stress and Poisson's ratio) for these two materials are presented in Table 1. Table 2 gives details of the loading conditions in the fatigue testing along with information on the crack length and cyclic life at which overloads were applied. It also gives the overload stress intensity factor and the calculated value of the Irwin monotonic plastic zone size for plane stress corresponding to the applied overloads. Constant amplitude fatigue loading with R = 0 was used to grow fatigue cracks from the notch (Table 2). A single polycarbonate specimen was used for the photoelastic work, with three sequential overloads of increasing magnitude being applied once data had been recorded for each overload and the crack had returned to pre-overload growth rates. The DIC part of the work used two aluminium specimens with different applied overload levels. The two different materials necessitated the use of two different servohydraulic testing machines, with the polycarbonate specimen being tested on a 25 kN machine (MTS model 370.02) at a frequency of 2 Hz (Figure 2a), while the aluminium specimens were tested on a 100 kN machine (MTS model 370.10) at a frequency of 10 Hz (Figure 2b). During the tests, fatigue cycling was periodically paused to allow the relevant digital images to be acquired through a load cycle.

For the transmission photoelasticity test, a circular polariscope was used to observe the fringe patterns using a monochromatic light source (Figure 2a). Images were acquired using a CCD camera (AVT, model Marlin F-146) placed perpendicularly to the specimen surface, equipped with a macro-zoom lens (MLH-10X EO) to increase the spatial resolution in the region around the crack tip. The field of view was 23.6 mm by 17.7 mm (giving a spatial resolution of 18.5 μm/pixel). The crack tip position was tracked by observing the fringe patterns captured during testing and the crack length was therefore measured from the relative difference between the position of the specimen notch and the crack tip.

Specimens for DIC work were prepared by spraying a black speckle pattern over a white background. Image acquisition utilised a CCD camera (AVT, model Stingray F-504B/C) placed perpendicularly to the speckled surface, focusing with a 75 mm lens (see Figure 2b). The field of view was 80.9 mm by 67.8 mm (giving a spatial resolution of 33 μm/pixel). An additional camera (AVT, model Pike F-032B/C) with a 25 mm lens was placed perpendicularly to the opposite side of the specimen to track the crack tip position and measure the crack length during fatigue tests (also shown in Figure 2b).

3.1 Determination of stress intensity factors

The aim of the present work is to correlate fatigue crack growth rates with accurate values of the effective stress intensity factor derived from the CJP model:

$$\Delta K_{CJP} = \left(K_{F,max} \pm K_{R,max}\right) - \left(K_{F,min} \pm K_{R,min}\right) \quad (1)$$

In equation 1, the ± indicates that K_F + $|K_R|$ was used when K_R was positive, and K_F - $|K_R|$ when K_R was negative. This distinction arises from the way that K_R is originally defined in terms of the coordinate axes, i.e. it characterises the direct stresses acting parallel to the crack growth direction and is obtained by evaluating σ_x in the limit as x → 0, along y = 0, i.e. towards the crack tip from behind along the crack flank. Thus in terms of the coordinate axes defining the cracked specimen, positive K_R values enhance crack growth and negative ones retard it. In the case of photoelasticity, calculation of the two stress intensity factors, K_F and K_R requires fitting experimental fringe order maps to the following stress field equation [18]:

$$\frac{Nf_\sigma}{t} = \sigma_1 - \sigma_2 = \left|\sigma_y - \sigma_x + 2i\sigma_{xy}\right| = \left|Az^{-\frac{1}{2}} + Bz^{-\frac{3}{2}}\bar{z} + Cz^0 + Dz^{-\frac{1}{2}}\ln z + Ez^{-\frac{3}{2}}\bar{z}\ln z\right| \quad (2)$$

The corresponding equation for DIC work is given by [19]:

$$2G(u+iv) = \varkappa\left[-2\left(B^{'} + 2E^{'}\right)z^{\frac{1}{2}} + 4E^{'}z^{\frac{1}{2}} - 2E^{'}z^{\frac{1}{2}}\ln z - \frac{C^{'}-F^{'}}{4}z\right] - z\left[-\left(B^{'} + 2E^{'}\right)\bar{z}^{-\frac{1}{2}} - E^{'}\bar{z}^{-\frac{1}{2}}\overline{\ln z} - \frac{C^{'}-F^{'}}{4}\right] - \left[A^{'}\bar{z}^{\frac{1}{2}} + D^{'}\bar{z}^{\frac{1}{2}}\overline{\ln z} - 2D^{'}\bar{z}^{\frac{1}{2}} + \frac{C^{'}+F^{'}}{2}\bar{z}\right] \quad (3)$$

Phase-stepping photoelasticity, as developed by Patterson and Wang [33] was adopted in this work, where six images of the fringe patterns for each load level were captured using equi-spaced angular orientations of the output quarter-wave plate and the analyser in the circular polariscope. These orientations together with the light intensity corresponding to each image are detailed in Table 3. In this table, i_m is an

intensity term representing the incoming external light in polariscope, i_v is the light intensity observed when the optical axes are parallel, δ is the relative retardation and γ is the isoclinic angle. Examples of the six fringe patterns obtained with the phase-stepping method for a crack length of 25.9 mm and a load level of 20 N are shown in Figure 3. In the DIC technique, a sequence of images were recorded at various load increments through complete loading and unloading cycles; this involved periodically pausing the fatigue cycling and incrementally loading the specimen whilst recording displacement images at each step.

Further processing of the images is necessary in either technique. As the CJP model is based on linear elastic fracture mechanics, the region around the crack that is plastically deformed has to be excluded from the analysis by applying a mask. The photoelastic phase-stepping method generates maps of relative retardation or isoclinic angle which are periodic and hence contain discontinuities and which must therefore be processed to obtain a continuous fringe pattern map. The first step in photoelastic image processing is to obtain the isoclinic map (equation 4) from the images 3 and 6 in Figure 3. The isoclinic fringes provide a map of principal stress directions over the chosen region in the specimen. The wrapped isochromatic map (equation 5), which represents the relative retardation of the light at each point in the specimen, was then obtained from the isoclinic map. The term wrapped refers to discontinuities of $\pi/2$ generated in the map due to the use of the arctangent operator in equation 5. Finally, an unwrapping process developed by Siegmann et al. [34] was applied to obtain a continuous fringe order map. Examples of the isoclinic, wrapped isochromatic and fringe order maps corresponding to a crack length of 25.9 mm and a load level of 20 N are shown in Figure 4.

Isoclinic map:
$$\gamma = \frac{1}{2}\tan^{-1}\frac{i_5 - i_3}{i_4 - i_6} \tag{4}$$

Wrapped isochromatic map:
$$\delta = \tan^{-1}\frac{(i_5 - i_3)\sin 2\gamma + (i_4 - i_6)\cos 2\gamma}{i_1 - i_2} \tag{5}$$

DIC images were processed using a cross-correlation algorithm [35] implemented in the commercial software package Vic-2D [36]. A facet size of 21 pixels with an overlap of 5 pixels was used to process the images. Figure 5 shows typical examples of the horizontal and vertical DIC displacement maps for a crack length of 35 mm and a load level of 600 N.

After obtaining either the fringe order maps or the displacement field images, the stress intensity factors defined in the CJP model can be found using a multi-point over-deterministic method developed by Sanford and Dally [37]. Since the CJP model is valid only in the near-tip elastic field region, a suitable annular region surrounding the crack tip had to be identified where valid experimental data could be obtained; Figure 6a illustrates this for the photoelastic case and Figure 6b shows an equivalent image for DIC data. This annulus is defined by two main parameters, an inner radius that is large enough to avoid including crack tip plastic deformation (based on a fracture mechanics calculation of the plastic zone size) and an outer radius defined to be within the region dominated by the elastic stress singularity and that is not influenced by specimen edge effects. Additionally, in the photoelastic work the measurement region is restricted by the mask applied around the crack to remove the plastically deformed enclave.

The region dominated by the crack tip singularity can be defined in the case of photoelasticity by the extent of the crack tip fringe loops, which is indicated by arrows on the maps in Figure 4. In DIC images, the vertical displacement map can be used to identify the outer radius of the annulus, by observing where the displacement field orientation becomes straight and perpendicular to the crack (indicated by the dashed lines in Figure 5b). Accuracy of the location of the crack tip position is important as it can have a significant effect on the calculations, and this position was optimised through a statistical assessment of the quality of the fit between the mathematical crack tip field solution and the experimental data, using the mean and variance. The appropriate crack tip position is regarded as that point in the image that gives the lowest values of the mean and the variance.

Processed image data can then be fitted to equations 2 and 3 in order to calculate the stress intensity factors K_F and K_R given by equations 6 and 7.

$$K_F = \sqrt{\frac{\pi}{2}(A' - 3B' - 8E')} \quad (6)$$

$$K_R = -(2\pi)^{\frac{3}{2}}E' \quad (7)$$

Equation 2 shows that the relationship between photoelastic fringe order and the unknown coefficients defined in the CJP model is nonlinear and hence the CJP coefficients A', B' etc were calculated by solving a nonlinear system of equations. The

solution of this nonlinear system used an iterative nonlinear least squares method in Matlab® software. However, equation 3 shows that the displacement fields are directly related to the CJP coefficients giving a linear system of equations to solve for the unknown CJP coefficients. An error function was defined for each technique (see equations 8 and 9) to optimise the fit between the experimental data and the mathematical expressions describing the crack tip fields. These error functions were minimised using a value of 10^{-5}.

Photoelasticity: $$g_{N,j} = f_{N,j}\left(A', B', C', D', E', F', z, f_\sigma, t\right) - N_j = 0 \quad (8)$$

DIC: $$\begin{Bmatrix} g_{u,j} \\ g_{v,j} \end{Bmatrix} = \begin{Bmatrix} f_{u,j}\left(A', B', C', D', E', F', z, G, \nu\right) \\ f_{v,j}\left(A', B', C', D', E', F', z, G, \nu\right) \end{Bmatrix} - \begin{Bmatrix} u_j \\ v_j \end{Bmatrix} = 0 \quad (9)$$

The subscript *j* indicates the values of the error function evaluated at the j^{th} data point with polar coordinates (r, θ).

4. Results and discussion

Figure 7 plots crack length against number of applied cycles for both the polycarbonate (Figure 7a) and aluminium specimens (Figure 7b). The retardation effect arising from certain overloads (Table 2) is clearly seen and it is also apparent this effect increases with an increase in overload ratio. The data for the polycarbonate specimen in Figure 7a indicate that only in the case of an overload of 200% of the previous constant amplitude maximum load was a retardation effect observed on crack propagation. The influence of this overload extended over 22000 cycles, which corresponded to a crack length increment of 1.3 mm. Overloads of 50% and 100% of the previous constant amplitude maximum load apparently did not affect the plastic enclave around the crack tip sufficiently to induce a retardation effect on crack growth rate. This is demonstrated in Figure 8 that compares, for all three overload cases, the photoelastic near-tip fringe patterns obtained at the minimum load in the fatigue cycle immediately prior to the overload (Figures 8a to 8c), with equivalent data recorded immediately after the overload (Figures 8d to 8f).In the case of the 50% and 100% overloads, there is little discernible difference between the fringe patterns recorded before and after the overload application(the overload plastic zone sizes calculated using the Irwin expression are r_p = 0.08 mm and r_p = 0.16 mm respectively – see Table 2). In contrast, for the 200% overload the plastic zone increases to r_p = 0.44 mm, leading to observable changes in the residual stresses present at the crack tip region at the minimum cyclic load (Figure 8f - marked with the arrow). Figure 7b shows equivalent crack length versus load cycles data for the two overloads applied to the aluminium

specimens. It can be seen that the retardation effect induced by a 100% overload (1.2 kN) extended over 135000 cycles (corresponding to a crack length increment of 2.1 mm); while the retardation subsequent to a 150% overload (1.35 kN) extended over 220000 cycles (corresponding to a crack length increment of 3.4 mm).

In order to calculate ΔK_{eff} values it was necessary to obtain values for the CJP stress intensity factors K_F and K_R. The interest here lies in investigating the ability of the CJP model to provide insight into the causes of crack growth rate changes attendant on an overload cycle, i.e. whether or not they can be explained solely by plasticity-induced shielding effects (wake contact and compatibility-induced residual stresses). Some previous work has indicated that accounting for overload effects may require consideration of ratcheting and use of a two parameter K_{max} and ΔK_{eff} characterisation of crack growth rate [5]–[7] that would reflect the operation of additional modes of fracture at higher peak loads and/or higher stress ratio values. Figure 9 shows the values calculated for K_F and K_R through the loading half-cycles occurring immediately prior to, and immediately after the overload cycle for the polycarbonate specimen (Figure 9a) and for the aluminium specimen (Figure 9b). It is clear in these figures that in most cases the application of an overload leads to a substantial increase in the magnitude of K_F at the minimum load in the cycle and a smaller increase in the magnitude of K_R at the minimum load. It is also clear that the change in slope of K_F and K_R occurs at a higher proportion of the loading half cycle indicating that crack tip shielding has increased and the value of ΔK_{eff} has decreased following the overload. It should be noted that the two smaller overloads applied to the polycarbonate specimen did not appear to produce a measurable retardation or shielding effect. Because the crack lengths associated with each overload in the single polycarbonate specimen were different, a different nominal stress intensity curve is followed in each case. In the two aluminium specimens, the overloads were applied at very similar crack lengths (Table 2) and the nominal stress intensity data lie on a single curve.

Equation 1 can be used to calculate values for the effective stress intensity range using the CJP model and Figure 10 shows the variation in ΔK_{eff} calculated with equation 1 as a function of crack length for all three CT specimens. It can be seen that the CJP model ΔK_{eff} values always lie below the ΔK_{nom} (defined using the standard Irwin stress intensity values [38], i.e. $\Delta K_{nom} = K_{max} - K_{min}$) and that an OL cycle leads to a reduction in the value of ΔK_{eff} and an associated decrease in crack growth rate (see Figure 11).

No overload effects were observed for the two lower overload values applied to the polycarbonate specimen, while in the case of the two aluminium specimens, a higher retardation effect was observed with a higher overload value.

The plasticity-induced shielding effect of an applied overload is more usefully illustrated by plotting the ratio between the effective and nominal ranges of stress intensity factor as a function of the crack length for both materials, as has been done in Figure 12. This figure shows several trends quite clearly; firstly, the level of plasticity-induced shielding is lower in the aluminium alloy under constant amplitude loading, i.e. the ratio of $\Delta K_{eff}/\Delta K_{nom}$ is higher at ≈0.85 – 0.90 than in the polycarbonate specimen (≈0.80). This can also be observed in the data presented in Figure 10 and is not a surprising observation, as the mechanisms of plastic deformation and shape of the plastic zones in the two materials are significantly different. PC undergoes crazing, that is similar to a Dugdale plastic zone [29], while aluminium alloys display a lobed shape resulting from slip mechanisms. The data from the two aluminium tests (CT2 100% OL and CT3 125% OL) also show that the higher overload leads to a greater reduction in the range of stress intensity after the overload. Values of $\Delta K_{eff}/\Delta K_{nom}$ immediately after the application of the overloads were approximately 0.63 for the polycarbonate specimen experiencing a 200% overload, and 0.7 and 0.59, respectively, for the aluminium specimens subject to 100% and 125% overloads.

These data can be re-plotted in the form of crack growth rate (da/dN) versus stress intensity factor range (ΔK) curves as has been done in Figure 13. Figure 13a shows typical ΔK_{eff} data, in this case for the polycarbonate specimen and a 200% OL (photoelastic measurements). The sequence of events during the overload has been numbered to indicate the various stages that occur. The initial period of constant amplitude crack growth is shown between points 1 and 2 where the values of ΔK_{eff} increase as expected. Once the overload is applied, however, there is a transient acceleration in the crack growth rate to point 3, followed by a substantial decrease in both crack growth rate and ΔK_{eff} to point 4. The period of crack growth retardation extends to point 5 as fatigue cycling continues, with a gradual increase in the crack growth rate being observed. From point 5 onwards the crack growth rate has recovered to follow the trend line associated with the previous constant amplitude loading. Figure 13b compares the crack growth rate curves plotted against the nominal applied values of ΔK and the effective values calculated using equation 1 for the aluminium specimens

(DIC measurements and R = 0). The nominal ΔK curve corresponds well with the data presented by Wanhill for 2.3 mm thick 2024-T3 bare plate for the same range of crack growth rates [38]. The effective stress intensity curve also correlates well with data presented by Newman, Phillips and Swain [39] for middle crack tension in 2.3 mm thick 2024-T3 plate at R=0, although the technique used to assess the effective stress intensity factor is not stated, as the data was drawn from other published work.

5. Effective stress intensity range from compliance traces

Compliance-based techniques have been widely used for measuring crack opening and closing loads [40]. The basic assumption is that contact between crack flanks results in a change of the specimen stiffness that is reflected in changes in the specimen compliance (or deflection per unit load).The interpretation of the effective range of stress intensity factor from compliance traces is, however, well known to have some drawbacks that have been discussed by many authors, e.g. [1], [41]–[43].In particular, Skorupa et al. [42] reported results from an extensive investigation of crack closure under constant amplitude, single spike and block overload tests at several load ratios, and considered the applicability of local compliance and notch extensometer techniques. They concluded that the method given in the ASTM standard [40] was the least subjective in identifying the crack closure level and insensitive to small amounts of measurement noise. They also noted a sensitivity of crack closure results to the level of offset used in compliance measurements and a dependence on load ratio. They concluded that the crack growth rate in the overload-affected zone that was predicted from crack closure measurements was in agreement with the observed crack growth rate, except for the period when crack growth rates were recovering from the slowest transient growth rate to the stabilised values. They attributed this observation to discontinuous closure where the fracture surfaces may touch some distance behind the crack tip, due to asperities or other protrusions on the fracture surfaces, despite the crack flanks being open near the crack tip.

The compliance technique does not incorporate any contribution to shielding that might arise from compatibility-induced stresses along the elastic-boundary boundary, while the CJP model assumes an exponential distribution of wake contact forces behind the crack tip and therefore does not consider the possibility of discontinuous wake contact. It is therefore of some interest to compare the analytical predictions of the CJP model

(which do include the possibility of a compatibility-induced contribution) with experimental data found using an extensometer.

The offset strain method was adopted in this work [44], using an extensometer to estimate the opening and closing loads from COD data recorded through specific fatigue cycles as a function of the applied load. In order to minimise measurement noise, the load-displacement signal was filtered with an incremental polynomial method similar to that described in ASTM E 647–00 [40]. The loading and unloading segments were plotted, and a least squares straight line was fitted to experimental data over the upper 25% of the loading or unloading trace. This straight line was extrapolated back to find estimated values of the opening (P_{op}) and closing (P_{cl}) loads from the load value at which a 2% strain offset occurred.

Figure 14 shows the compliance traces recorded during the load cycles immediately before and immediately after the spike overload for the aluminium specimen. The figure caption indicates which plots relate to either loading or unloading half-cycles. Prior to the overload application, opening and closing loads of 100 N and 110 N were measured with the offset compliance technique from the analysis of the loading (Figure 14c) and unloading (Figure 14d) half-cycles. In contrast, for the cycle immediately after the overload, the corresponding load values were 255 N (Figure 14g) and 260 N (Figure 14h). However, the interpretive difficulties of using the compliance technique to assess the effective stress intensity factor range are made clear in a comparison of the measured compliance data in Figures 14a, 14b, 14e and 14f with the offset data in Figures 14c, 14d, 14g and 14h. The offset curves are not bilinear and reflect both the extent of plasticity in their upper part and the possibility of crack unzipping and discontinuous closure.

The data shown in Figure 14 can be processed to obtain values of ΔK_{eff} and the ratio of $\Delta K_{eff}/\Delta K_{nom}$ plotted to illustrate the influence of changes in opening load on the effective stress intensity factor as the crack grows through the overload-affected region, as has been done in Figure 15 for both aluminium specimens. It is clear that under constant amplitude loading this ratio averages ≈ 0.82, corresponding to P_{op} values of approximately 100 N. Similar behaviour, where opening and closing loads remain unchanged with increasing crack length, has been reported by Sehitoglu [45], McClung and Sehitoglu [46] and Wei and James [47]. Figure 15 shows that $\Delta K_{eff}/\Delta K_{nom}$ values

decrease sharply, immediately after the application of the overload, reflecting an increase in closure load, followed by a progressive increase over a distance of several millimetres, until they reach similar values to those that existed before the overload. The magnitude of the decrease in ΔK_{eff} (equivalent to an increase in P_{op}) depends on the overload level; for a 100% overload (Al_CT2), a 35.2% increase in P_{op} to 211 N was observed. In this case, the Irwin plastic zone size was r_p = 0.58 mm and the crack growth rate retardation extended over 2.1 mm (equivalent to 3.6r_p). For the 125% overload (Al_CT3), P_{op} increased by 42.7% to 256 N; the Irwin plastic zone size was 0.77 mm and the retardation extended over a crack increment of 3.4 mm, or 4.4r_p.This reflects the enhanced shielding effect arising from the larger plastic zone associated with the higher overload. However, there is no simple relationship between overload plastic zone size and the resulting effects on crack growth rate. This implies that shielding influence is not simply a wake contact effect but reflects other influences with a more sustained effect on crack growth rate. The current view of the present authors is that these other influences may include compatibility-induced residual strains that are included in the CJP model of crack tip stresses and the possibility of both ratcheting and the necessity of using a two parameter K_{max} and ΔK_{eff} characterisation of crack growth rate.

Figure 16 shows, for the two aluminium specimens CT2 and CT3, a comparison between ΔK_{eff} found using K_F and K_R calculated from the CJP model (equation 1) and the value found using the offset strain method. Whilst at first glance, it may appear that a good correlation is obtained between the results obtained from the two methods, a closer inspection shows that in both specimens the values of ΔK_{eff} found using the compliance technique are lower than those found from the CJP model. This observation appears counter to the initial expectation that, as the CJP model includes compatibility effects, use of equation 1 would lead to lower values of ΔK_{eff}, i.e. higher plasticity-induced shielding, compared with the compliance data. However, several points are worth noting in this respect; firstly, as observed by Skorupa et al. [42] in their conclusions, compliance is variable over the whole load range, even when the crack is open, and any such additional curvature can change the observed opening or closing point in the compliance trace, i.e. compliance is not a reliable method of assessing the effective value of stress intensity factor. Skorupa et al. [42] also compared their measured transient crack growth rate data during an OL with predictions inferred from applying their crack closure measurements to the constant amplitude *da/dN* versus ΔK_{eff} growth rate curve. The observed crack growth rates were consistently

considerably higher than the predicted values. This indicates that the compliance technique leads to an overestimate of closure compared with the true value. Secondly, the formulation of the CJP model allows for K_R to either retard or assist crack growth, depending on the direction of the various stresses included in the model. Thus the higher values of ΔK_{eff} observed during the overload cycle and subsequently, compared with the compliance values, may well reflect the influence of the change in compatibility-induced strains arising from the higher applied load. The ΔK_{eff} data derived from the CJP model seen in Figure 16 are slightly higher than the compliance data which would lead to higher growth rates and is therefore consistent with the observations made by Skorupa et al. [42].

As mentioned in section 2, the CJP model of crack tip fields offers the possibility of obtaining insight into the mechanisms underlying the plasticity-induced shielding phenomenon. This is possible because the relative contributions and influence that arise from *T*-stress, crack wake contact, compatibility-induced strains at the elastic-plastic interface or from fracture surface roughness can, in principle, be explored by varying the values of the independent parameters in the appropriate terms in the mathematical model [22], and by examining changes in the various coefficients of the terms in the model (e.g. *A*, *B* and *E*). The concept is illustrated in Figure 17, which presents data for the parameters *A*, *B* and *E* obtained from two aluminium specimens during a loading half cycle applied immediately before the overload and immediately after the overload. The value of K_R is a function of the parameter *E*, which Figure 17c indicates generally reduces in value after the overload. *E* is a parameter that describes the stress field along the crack flanks, taking account of wake contact. This observation therefore supports the argument made in the preceding paragraph, as to the cause of the CJP model values of ΔK_{eff} being higher than the compliance values. K_F is a function of *A, B* and *E* and considers both crack flank contact and compatibility-induced interfacial shear stresses through the sum of *A* + *B* [18]. Changes in the sum *A* + *B* can be seen in Figure 17d where significant changes can be clearly observed in this sum after the overload, with values higher in the lower part of the fatigue cycle and lower over the majority of the load cycle. The full interpretation of this type of data is currently in progress by the present authors, but its relevance to the mechanisms underlying the growth rate changes observed during an overload cycle is clear.

6. Conclusions

The work described in the present paper deals with a quantitative evaluation of the fatigue crack retardation effects following application of single overloads. The CJP model stress intensity factors, K_F and K_R, have been measured on a 2 mm thick polycarbonate compact tension specimen via photoelasticity and on two similar aluminium CT specimens by a digital image correlation technique. These two stress intensity factors were then used to calculate the effective range of stress intensity factor (equation 1). The values of ΔK_{eff} found using DIC and the CJP model of crack tip fields were then compared with those determined from a compliance-based technique. The compliance technique was found to underestimate the effective stress intensity factor range, compared with the CJP model. The CJP model partitions the various stresses acting at the notional elastic-boundary boundary into a stress intensity factor K_F that drives crack growth and is analogous to K_I, although it also includes stress components reflecting wake contact and compatibility-induced strains, and a retarding stress intensity factor K_R that can either assist crack growth or retard it and which acts along the plane of the crack. Changes in these two stress intensity factors through an overload cycle derive from changes to the stress components and these changes can be followed through observing the changes in the stress fitting parameters *A, B*, and *E* used in the model and which define K_F and K_R. The sum $A + B$ is a representation of the interfacial shear stresses induced along the elastic-plastic boundary while *E* reflects wake contact. Changes in K_R therefore explicitly indicate how wake contact stresses change during and after an overload and, depending on whether K_R is positive or negative in sign, it may enhance crack growth or retard it. Once accurate values of ΔK_{eff} can be determined it becomes possible to explore whether overload effects can only be understood through consideration of additional influences such as ratcheting or a two parameter characterisation of crack growth rate (K_{max} and ΔK). The CJP model of crack tip fields appears to offer significant new opportunities in this respect.

Acknowledgements

This work has been conducted with financial support from Gobierno de España through the project ‘Proyecto de Investigación de Excelencia del Ministerio de Economía y Competitividad MAT2016-76951-C2-1-P’.

References

[1] M.N. James, Some unresolved issues with fatigue crack closure–measurement, mechanism and interpretation problems, Advances in Fracture Research,

Proceedings of the Ninth International Conference on Fracture, Sydney, (eds. B L Karihaloo et al), Australia, Pergamon Press 5 (1997) 2403–2414.

[2] J. Schijve, Some formulas for the crack opening stress level, Eng. Fract. Mech. 14 (1981) 461-465.

[3] R. Pippan, A. Hohenwarter, Fatigue crack closure: a review of the physical phenomena, Fatigue Fract. Eng. Mater. Struct. 40 (2017) 471–495.

[4] C.S. Shin, S.H. Hsu, On the mechanisms and behaviour of overload retardation in AISI-304 stainless steel, Int. J. Fatigue 15 (1993) 181–192.

[5] Zhenyu Ding, Xiaogui Wang, Zengliang Gao and Shiyi Bao, An experimental investigation and prediction of fatigue crack growth under overload/underload in Q345R steel, Int. J. Fatigue 98 (2017) 155-166.

[6] A.K. Vasudevan, K. Sadananda, N. Louat, A review of crack closure, fatigue crack threshold and related phenomena, Mat. Sci. Eng. A188 (1994) 1–22.

[7] K. Sadananda, A.K. Vasudevan, R.L. Holtz, E.U. Lee, Analysis of overload effects and the related phenomena, Int. J. Fatigue 21 (1999) S233–S246

[8] R.C. Alderliesten, How proper similitude can improve our understanding of crack closureand plasticity in fatigue, Int. J. Fatigue 82 (2016) 263-273.

[9] E.A. Patterson, Digital photoelasticity: Principles, practice and potential, Strain 38 (2002) 27–39.

[10] B. Pan, K. Qian, X. Huimin, A. Asundi, Two-dimensional digital image correlation for in-plane displacement and strain measurement: a review, Meas. Sci. Technol. 20 (2009) 1–17.

[11] M. Janssen, J. Zuidema, R.J.H. Wanhill, Fracture Mechanics, Spon Press, Abingdon, UK, 2006.

[12] M.L. Williams, On the stress distribution at the base of a stationary crack, J. Appl. Mech. 24 (1957) 109–114.

[13] N.I. Muskhelishvili, Some Basic Problems of the Mathematical Theory of Elasticity, Noordhoff International Publishing, Groningen, The Netherlands, 1977.

[14] K. Ramesh, S. Gupta, A.A. Kelkar, Evaluation of stress field parameters in fracture mechanics by photoelasticity–revisited, Eng. Fract. Mech. 56(1) (1997) 25–45.

[15] A.D. Nurse, E.A. Patterson, Determination of predominantly mode II stress intensity factors from isochromatic data, Fatigue Fract. Eng. Mater. Struct. 16(12) (1993) 1339–1354.

[16] J.R. Yates, M. Zanganeh, Y.H. Tai, Quantifying crack tip displacement fields with DIC, Eng. Fract. Mech. 77 (2010) 2063–2076.

[17] P. López-Crespo, A. Shterenlikht, E.A. Patterson, P.J. Withers, J.R. Yates, The stress intensity factors of mixed mode cracks determined by digital image correlation, J. Strain Anal. Eng. Des. 43 (2008) 769–780.

[18] C.J. Christopher, M.N. James, E.A. Patterson, K.F. Tee, Towards a new model of crack tip stress fields, Int. J. Fract. 148 (2007) 361–371.

[19] M.N. James, C.J. Christopher, Y. Lu, E.A. Patterson, Local crack plasticity and its influences on the global elastic stress field, Int. J. Fatigue 46 (2013) 4–15.

[20] J.M. Vasco-Olmo, M.N. James, C.J. Christopher, E.A. Patterson, F.A. Díaz, Assessment of crack tip plastic zone size and shape and its influence on crack tip shielding, Fatigue Fract. Eng. Mater. Strcut. 39 (2016) 969–981.

[21] C.J. Christopher, M.N. James, E.A. Patterson, K.F. Tee, A quantitative evaluation of fatigue crack shielding forces using photoelasticity, Eng. Fract. Mech. 75 (2008) 4190–4199.

[22] C.J. Christopher, G. Laboviciute, M.N. James, E.A. Patterson, Extension of the CJP model to mixed mode I and mode II, Frattura ed Integrita Strutturale 7 (2013) 161–166.

[23] D. Nowell, K.I. Dragnevsky, S.J. O'Connor, Investigation of fatigue crack models by micro-scale measurement of crack tip deformation, Int. J. Fatigue (2018), in press Special Issue on Crack Tip Fields 4, Corsica, April, 2017, September issue of Int. J. Fatigue.

[24] M.N. James, J.F. Knott, An assessment of crack closure and the extent of the short crack regime in Q1N (HY 80) steel, Fatigue Fract. Eng. Mater. Struct. 8 (1985) 177–191.

[25] M.N. James, M.N. Pacey, L.W. Wei, E.A. Patterson, Characterisation of plasticity-induced closure – crack flank contact force versus plastic enclave, Eng. Fract. Mech. 70 (2003) 2473–2487.

[26] J.M. Vasco-Olmo, F.A. Díaz, Experimental evaluation of plasticity-induced crack shielding from isochromatic data, Opt. Eng. 54(8) (2015) doi: 10.1117/1.OE.54.8.081203.

[27] B. Yang, J.M. Vasco-Olmo, F.A. Díaz, M.N. James, A more effect rationalisation of fatigue crack growth rate data for various specimen geometries and stress ratios using the CJP model, Int. J. Fatigue 114 (2018), 189–197.

[28] J.M. Vasco-Olmo, F.A. Díaz, A. García-Collado, R. Dorado, Experimental evaluation of crack shielding during fatigue crack growth using digital image correlation, Fatigue Fract. Eng. Mater. Struct. 38(2) (2013) 223–237.

[29] M.N. James, C.J. Christopher, Y. Lu, E.A. Patterson, Fatigue crack growth and craze-induced crack tip shielding in polycarbonate, Polymer 53 (2012) 1558–1570.

[30] C. Colombo, Y. Du, M.N. James, E.A. Patterson, L. Vergani, On crack tip shielding due to plasticity-induced closure during an overload, Fatigue Fract. Eng. Mater. Struct. 33 (2010) 766–777.

[31] D. Nowell, M.E. Kartal, P.F.P. de Matos, Digital image correlation measurement of near-tip fatigue crack displacement fields: constant amplitude loading and load history effects, Fatigue Fract. Eng. Mater. Struct. 36 (2012) 3–13.

[32] P. López-Crespo, P.J. Withers, F. Yusof, H. Dai, A. Steuwer, J.F. Kelleher, T. Buslaps, Overload effects on fatigue crack-tip fields under plane stress conditions: surface and bulk analysis, Fatigue Fract. Eng. Mater. Struct. 36(1) (2013) 75–84.

[33] E.A. Patterson, Z.F. Wang, Towards full-field automatic photoelastic analysis of complex components, Strain 27 (1991) 49–56.

[34] P. Siegmann, D. Backman, E.A. Patterson, A robust approach to demodulating and unwrapping phase-stepped photoelastic data, Soc. Exp. Mech. 45(3) (2005) 278–289.

[35] M.A. Sutton, J.J. Orteu, H.W. Schreier, Image Correlation for Shape, Motion and Deformation Measurements: Basic Concepts, Theory and Applications, Springer Science + Business Media, New York, 2009.

[36] http://www.correlatedsolutions.com/vic-2d/

[37] R.J. Sanford, J.W. Dally, A general methodology for determining the mixed-mode stress intensity factors from isochromatic fringe patterns, Eng. Fract. Mech. 11 (1979) 621–633.

[38] R.J.H. Wanhill, Low stress intensity fatigue crack growth in 2024-T3 and T351, Eng. Fract. Mech. (1988) 233-260.

[39] J.C. Newman, Jr, E.P. Phillips and M.H. Swain, Fatigue-life prediction methodology using small-crack theory, Int. J. Fatigue 21 (1999) 109-119.

[40] E 647–00, Standard Test Method for Measurement of Fatigue Crack Growth Rates, Philadelphia: American Society For Testing and Materials, 2000.

[41] T.T. Shih, R.P. Wei, A study of crack closure in fatigue, Eng. Fract. Mech. 6 (1974) 19–32.

[42] M. Skorupa, T. Machniewicz, A. Skorupa, Applicability of the ASTM compliance offset method to determine crack closure levels for structural steel, Int. J. Fatigue 29 (2007), 1434–1451.

[43] J.H. Song, Y.I. Chung, A review of crack closure measurement by compliance technique and the normalised- extended ASTM method as a currently most refined, practical and dimple one, Procedia Engineering 2 (2010), 777–786.

[44] S. Stoychev, D. Kujawski, Methods for crack opening load and crack tip shielding determination: a review, Fatigue Fract. Eng. Mater. Struct. 26 (2003) 1053–1067.

[45] R.C. Sehitoglu, Crack opening and closure in fatigue, Eng. Fract. Mech. 21(2) (1985) 329–339.

[46] R.C. McClung, H. Sehitoglu, On the finite element analysis of fatigue crack closure – 2 Numerical results, Eng. Fract. Mech. 33(2) (1989) 253–272.

[47] L.-W. Wei, M.N. James, A study of fatigue crack closure in polycarbonate CT specimens, Eng. Fract. Mech. 66 (2000) 223–242.

Tables

Mechanical property	Unit	Value	
		Polycarbonate	Al2024-T3
Young's modulus	MPa	2350	73000
Yield stress	MPa	60	345
Poisson's ratio	-	0.38	0.33

Table 1. Mechanical properties for the polycarbonate and 2024 aluminium alloy used in this work.

Optical technique	Specimen reference	Loading conditions		Overload conditions					
		P_{min} (N)	P_{max} (N)	Percentage (%)	P_{OL} (N)	a_{OL} (mm)	N_{OL} (cycles)	K_{OL} (MPa·m$^{1/2}$)	r_p (mm)
Transmission photoelasticity	PC_CT1	0	50	50	75	26.7	120000	0.93	0.08
				100	100	28.9	145000	1.35	0.16
				200	150	31.1	167500	2.20	0.44
DIC	Al_CT2	5	600	100	1200	26.1	280000	14.67	0.58
	Al_CT3			125	1350	26.7	200000	16.98	0.77

Table 2. Experimental conditions defined for the fatigue tests.

Image	Angle of output quarter-wave plate (rad)	Angle of analyser (rad)	Light intensity
1	0	π/4	$i_1 = i_m - i_v \cos\delta$
2	0	-π/4	$i_2 = i_m + i_v \cos\delta$
3	0	0	$i_3 = i_m - i_v \sin\delta \sin 2\gamma$
4	π/4	π/4	$i_4 = i_m + i_v \sin\delta \cos 2\gamma$
5	π/2	π/2	$i_5 = i_m + i_v \sin\delta \sin 2\gamma$
6	3π/4	3π/4	$i_6 = i_m - i_v \sin\delta \cos 2\gamma$

Table 3. Angular orientations of both the output quarter-wave plate and the analyser and light intensities of each image for implementing Patterson and Wang's phase-stepping method [33].

Figures

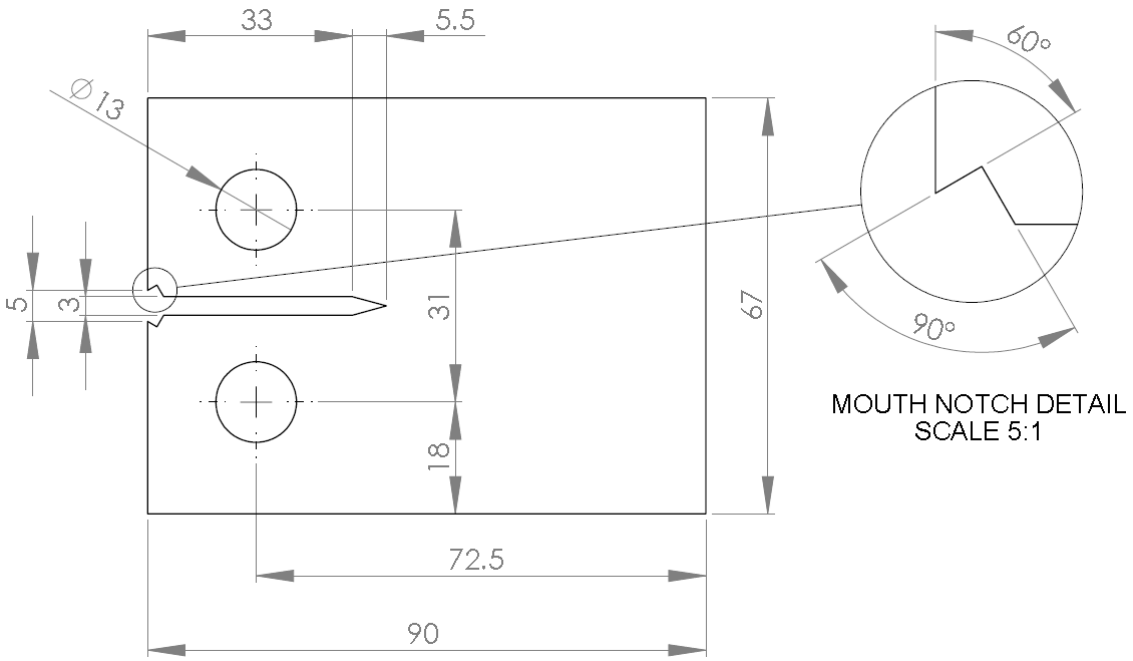

Figure 1 Geometry and dimensions (mm) of the 2 mm thick compact tension specimens used in this work.

Figure 2 Experimental setup used to measure (a) isochromatic fringe patterns by transmission photoelasticity and (b) displacement fields by DIC.

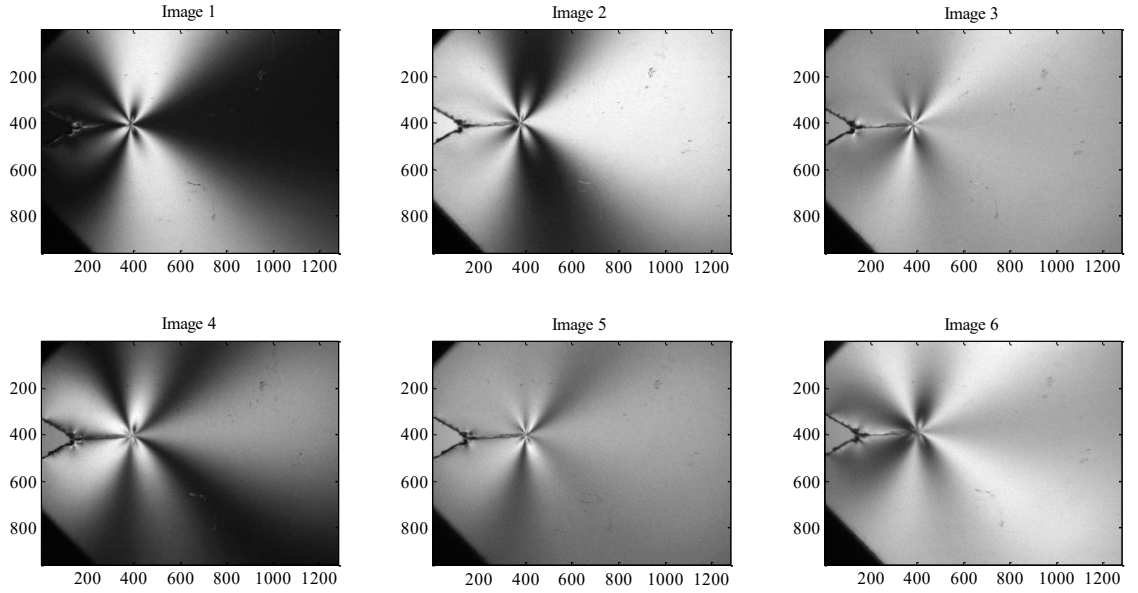

Figure 3 Example of fringe patterns corresponding to the six images defined in Table 3, for a crack length of 25.9 mm and a load level of 20 N obtained with the phase-stepping method developed by Patterson and Wang [33].

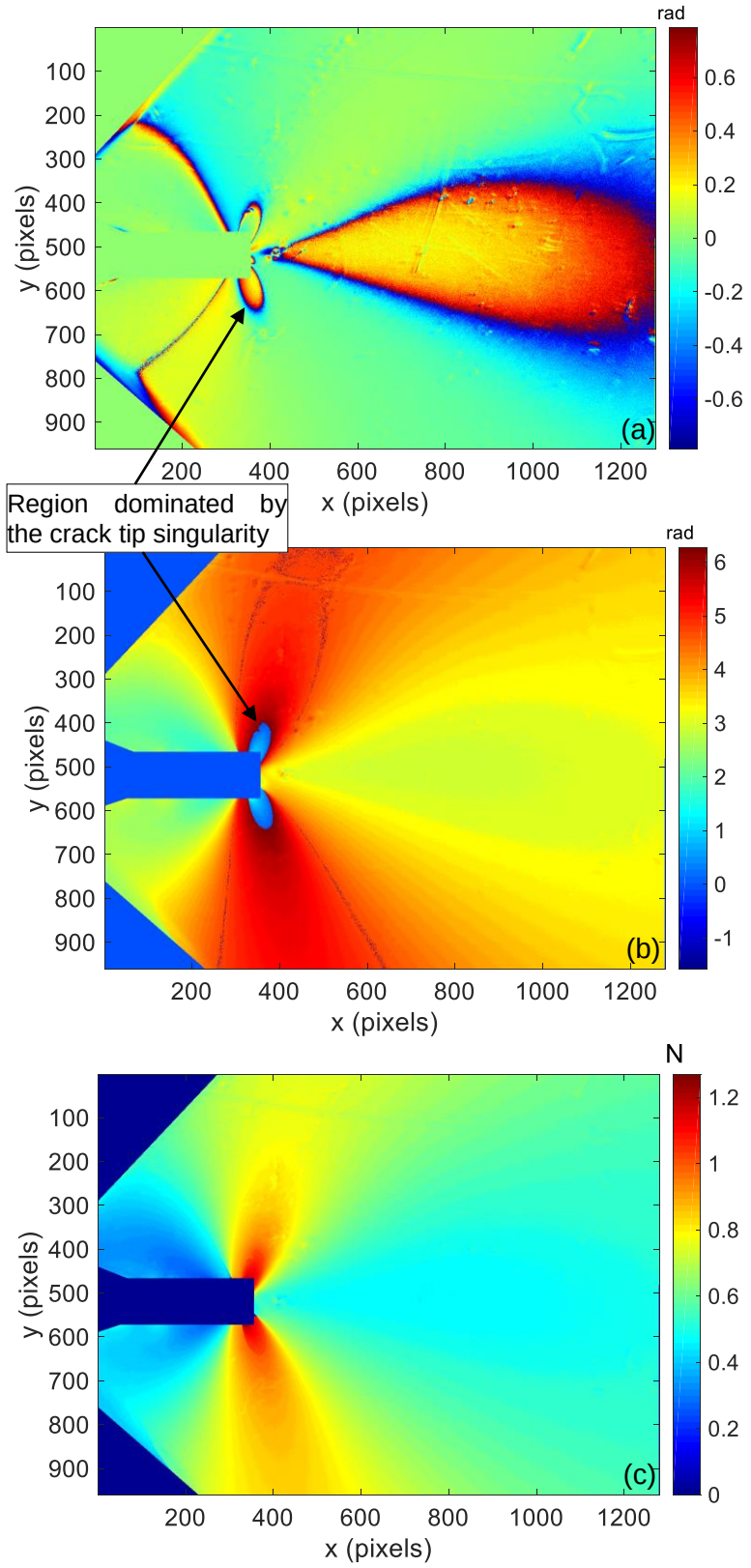

Figure 4 Examples of photoelastic images of (a) isoclinic map, (b) wrapped isochromatic map and (c) fringe order map corresponding to a crack length of 25.9 mm and a load level of 20 N. The border of the region dominated by the crack tip singularity is indicated by arrows.

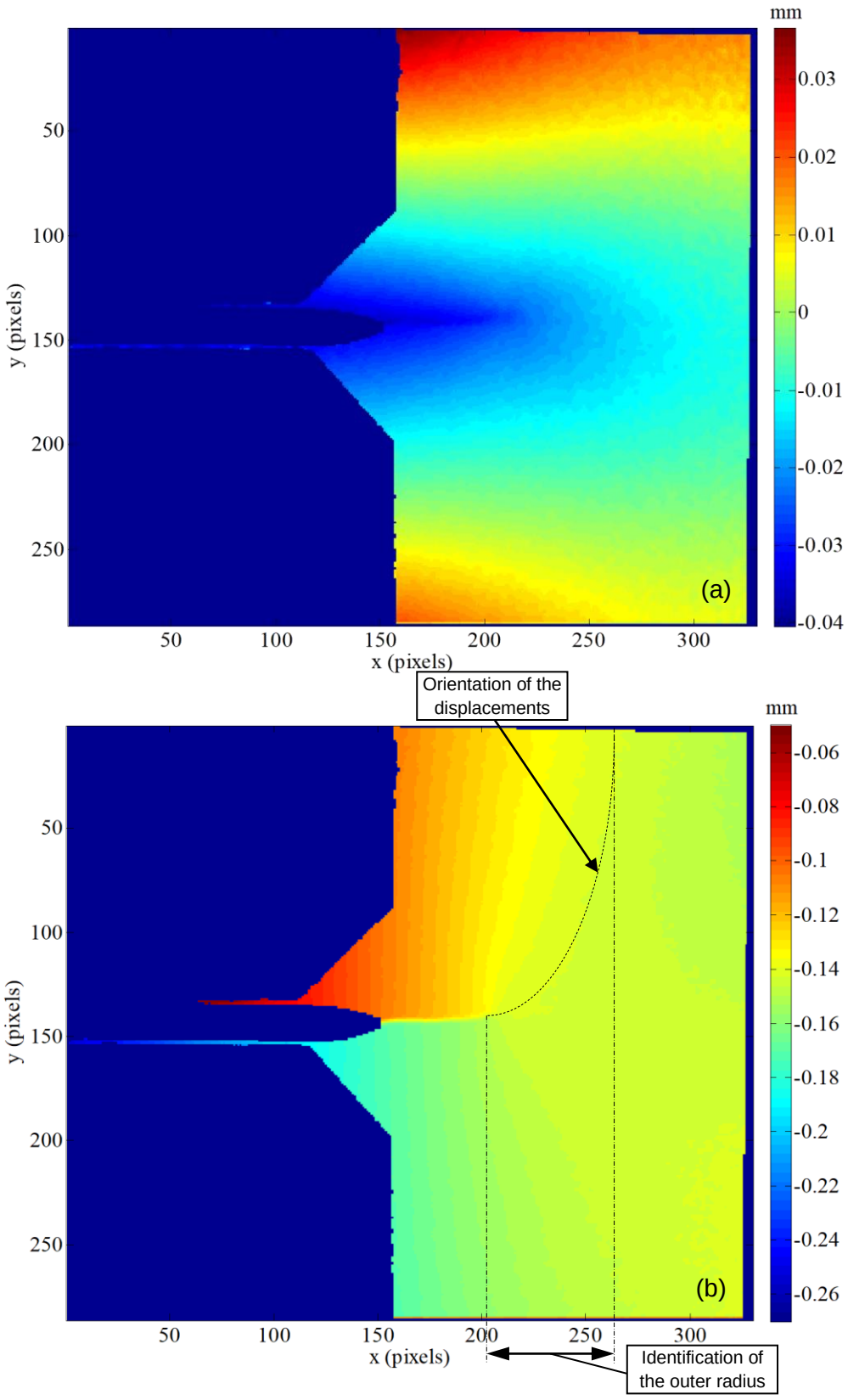

Figure 5 (a) Horizontal and (b) vertical displacement fields measured with DIC for a crack length of 35 mm and a load level of 600 N.

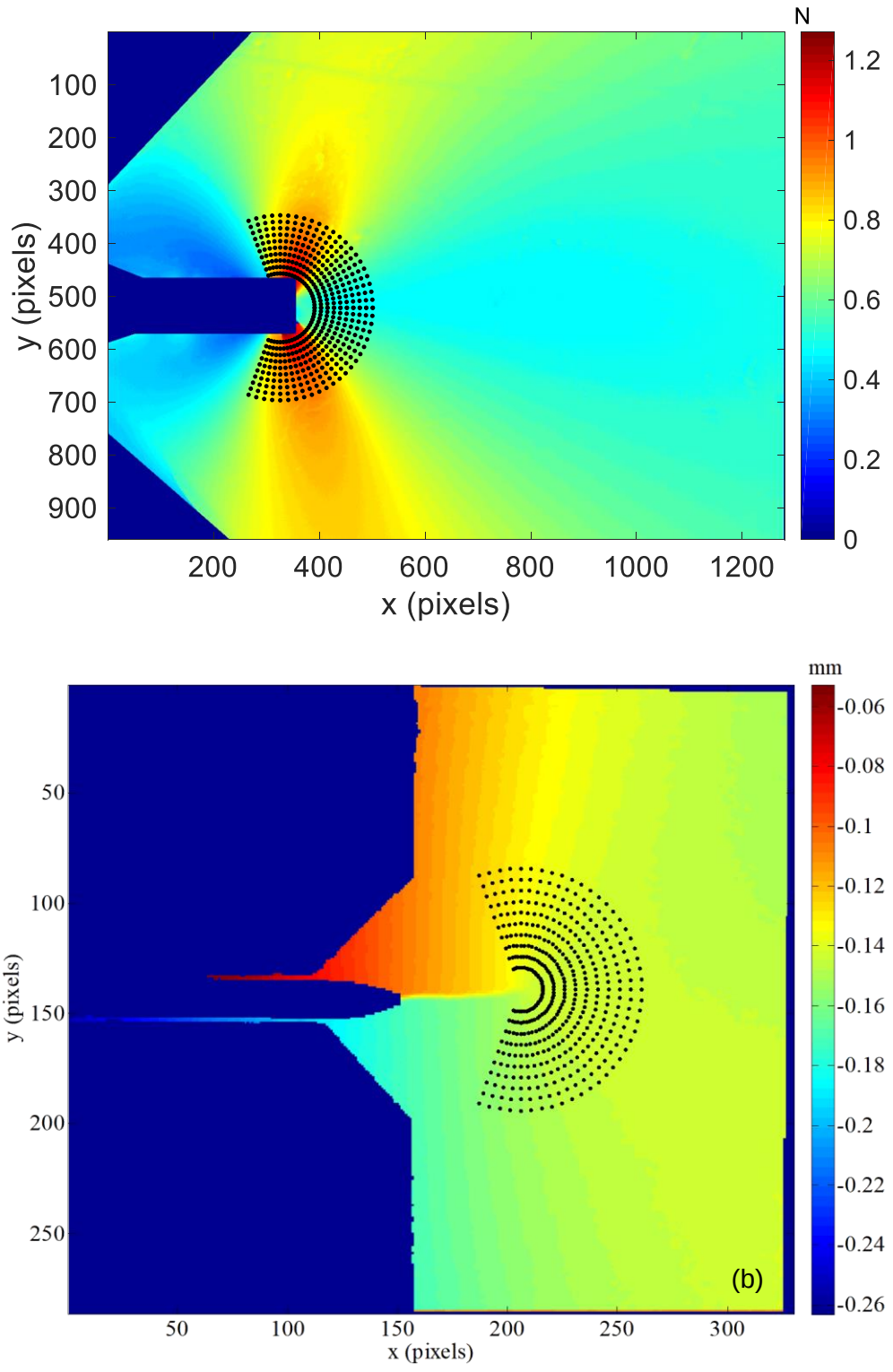

Figure 6 Annular mesh of data points used to calculate the CJP model stress intensity factors. (a) Photoelastic fringe order map (a = 25.9 mm, P = 20 N) and (b) DIC vertical displacement field (a = 35 mm, P = 600 N).

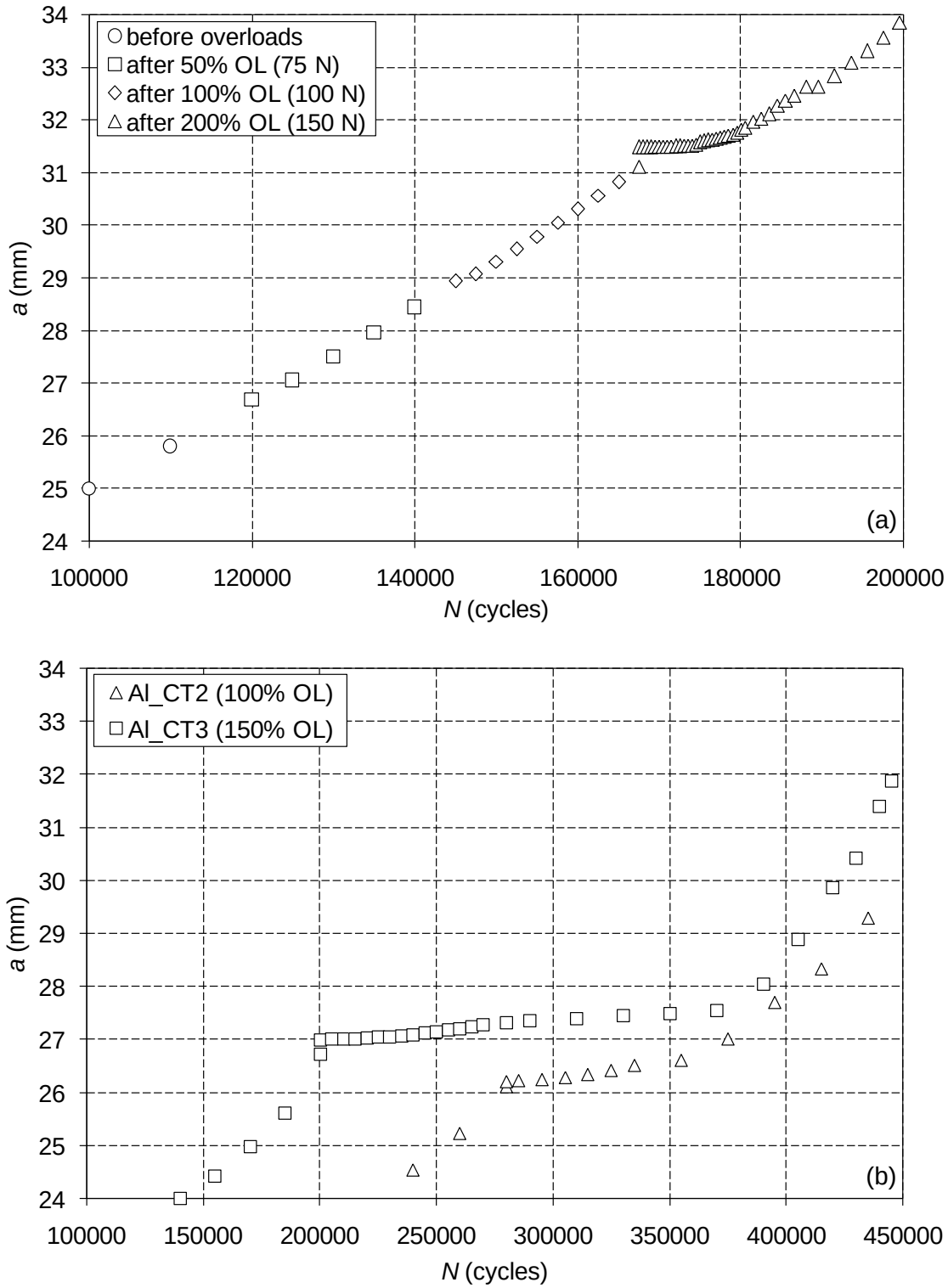

Figure 7 Crack length as a function of the number of load cycles for the specimens subjected to multiple single overload cycles: (a) Polycarbonate and (b) Al2024-T3 specimens.

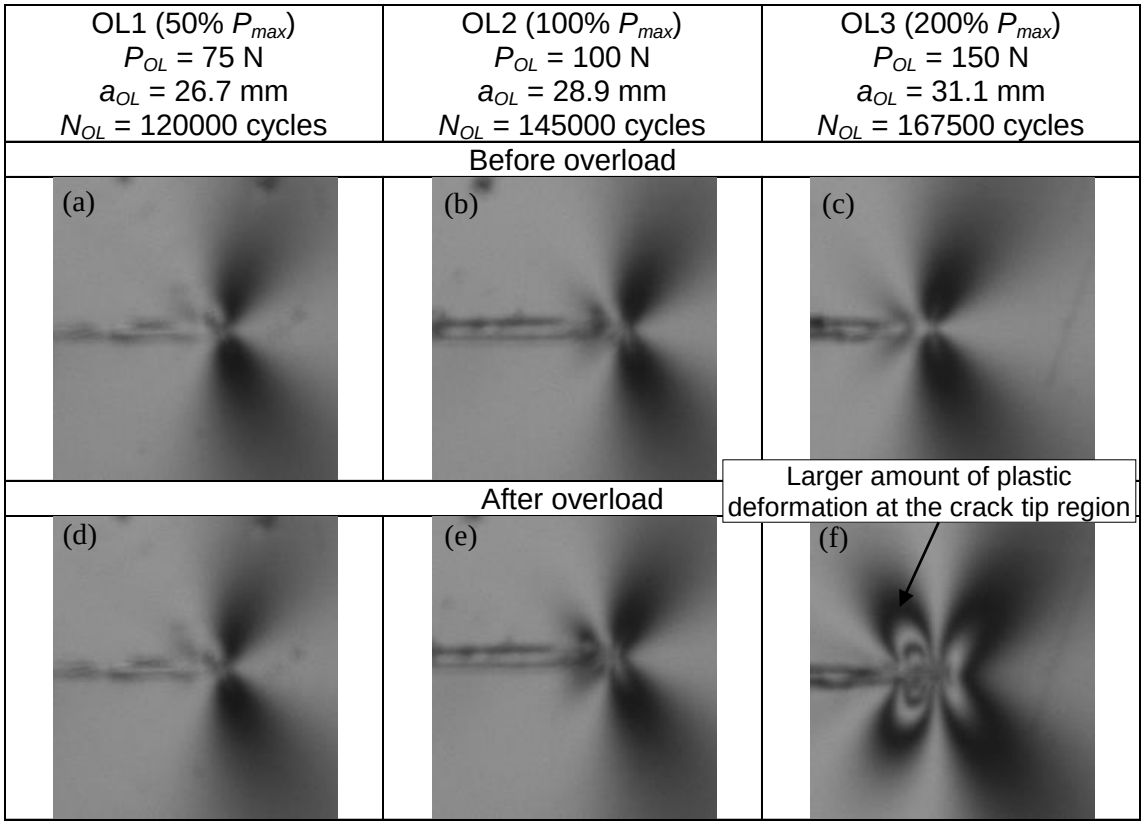

Figure 8 Light background fringe patterns corresponding to the three values of overload (50%, 100% and 200%) applied to the polycarbonate specimen one cycle before and after their application.

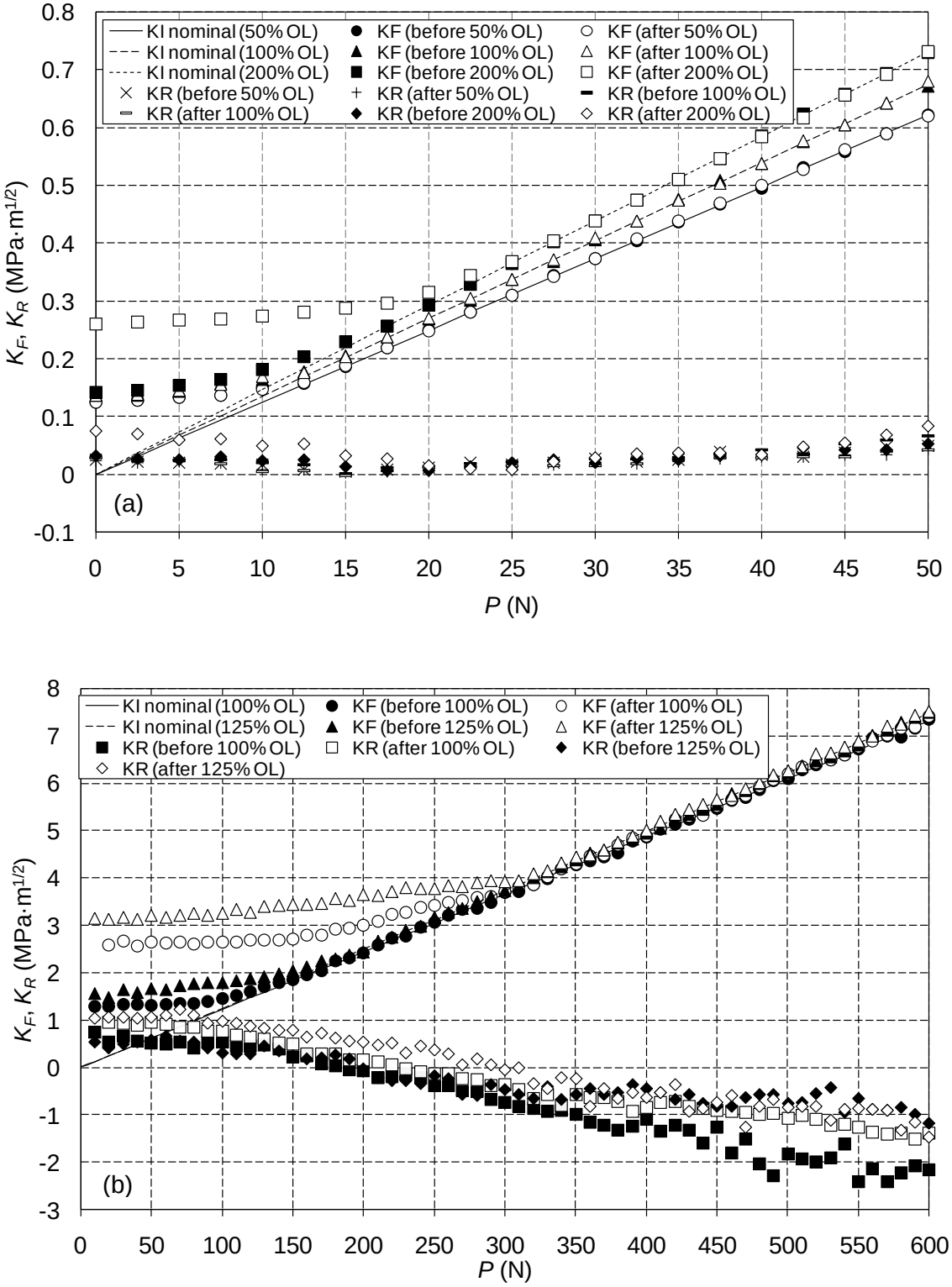

Figure 9 K_F and K_R values though the loading half-cycles immediately before (black symbols) and after (white symbols) the applied overload corresponding to: (a) polycarbonate specimen under 50%, 100% and 200% overloads and (b) aluminium specimens under 100% and125% overloads.

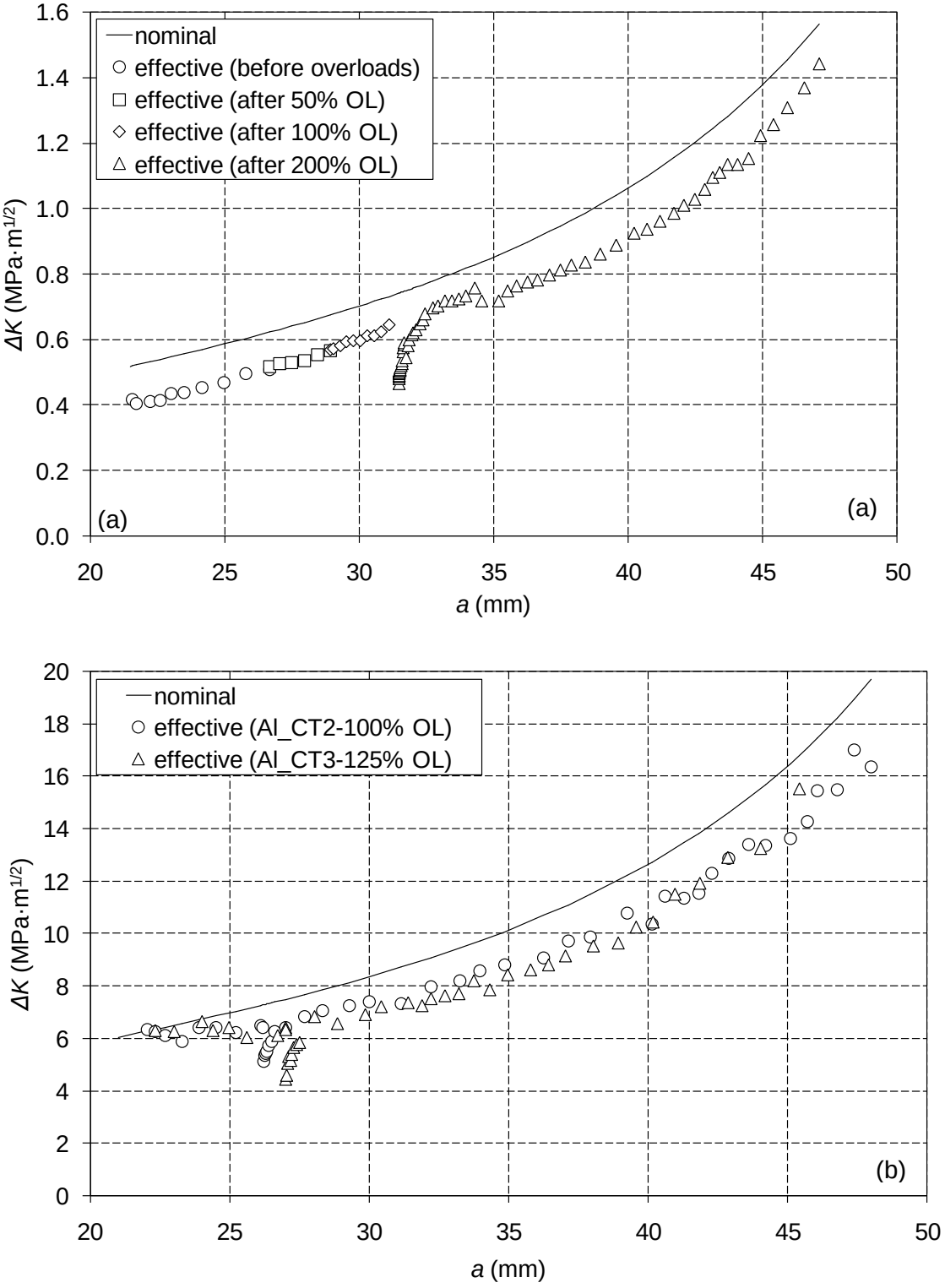

Figure 10 Variation in ΔK_{eff} (calculated from equation 1) with crack length for all three CT specimens. (a) Polycarbonate specimen and (b) Aluminium specimens.

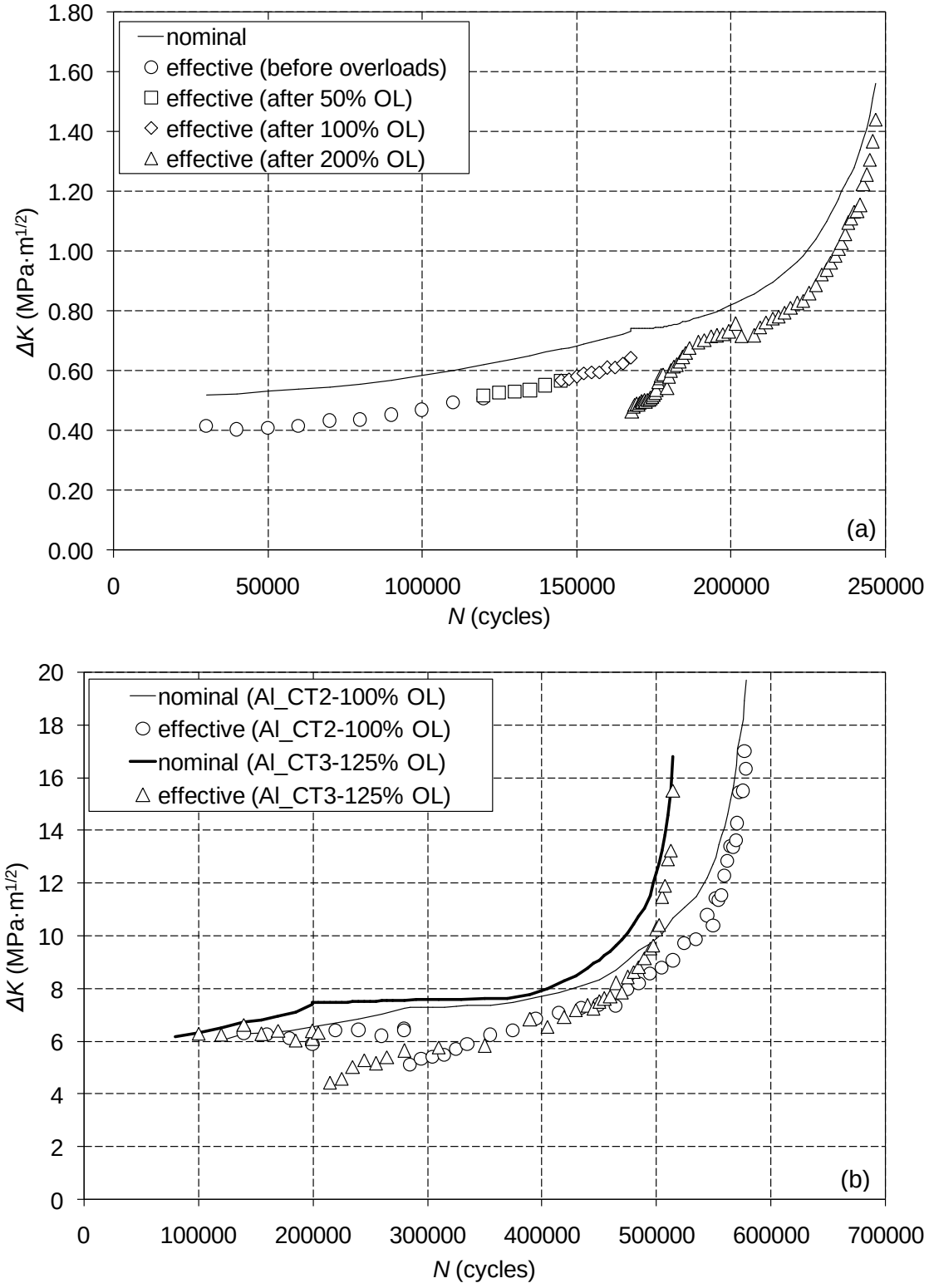

Figure 11 Variation in the CJP model values of ΔK_{eff} with the number of applied cycles for all the CT specimens. (a) Polycarbonate specimen and (b) Aluminium specimens.

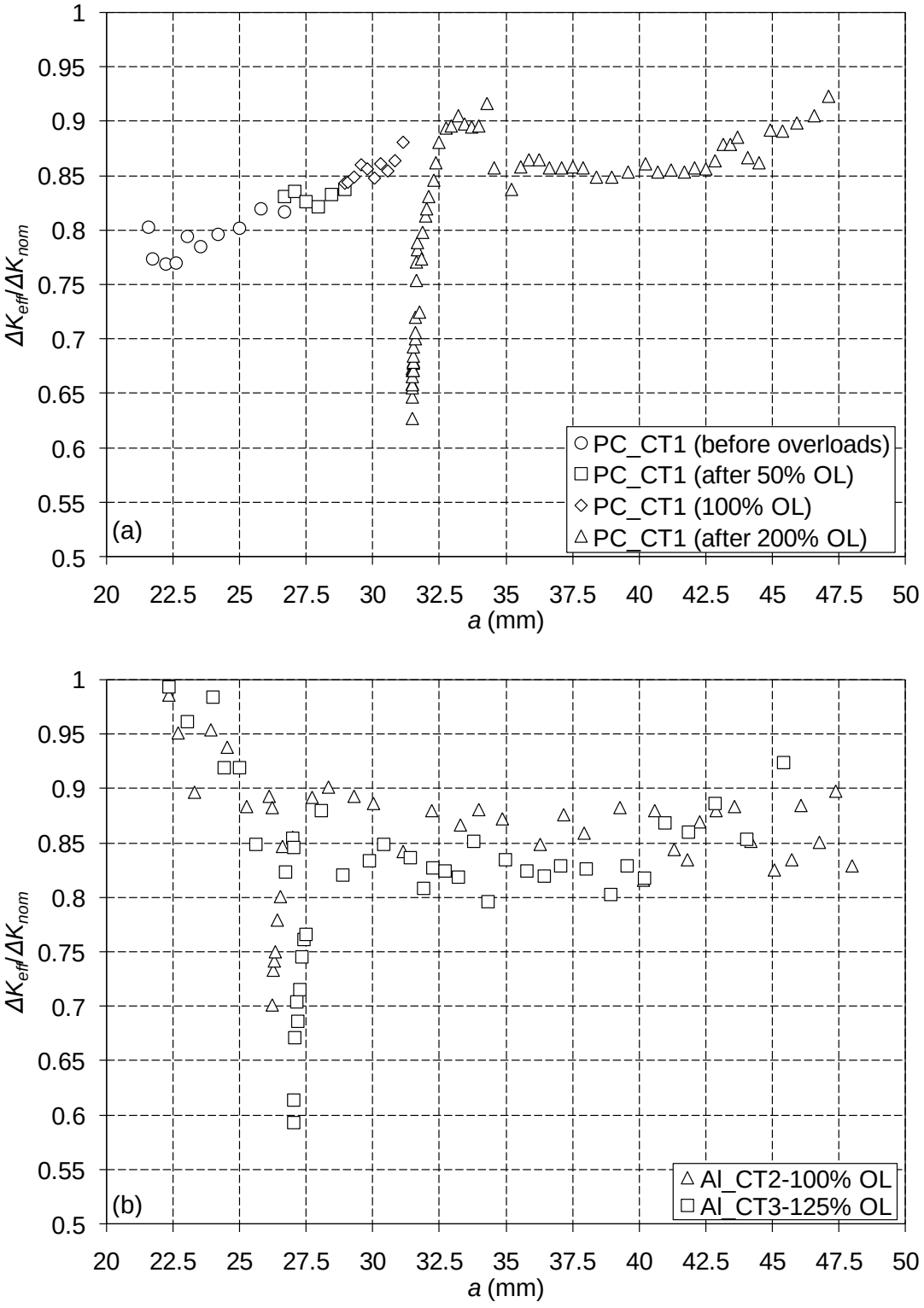

Figure 12 Variation in the ratio $\Delta K_{eff}/\Delta K_{nom}$ with crack length for all three CT specimens tested, identified as: (a) Polycarbonate (PC_CT1), and (b) aluminium (Al_CT2–100% OL and Al_CT3–125% OL).

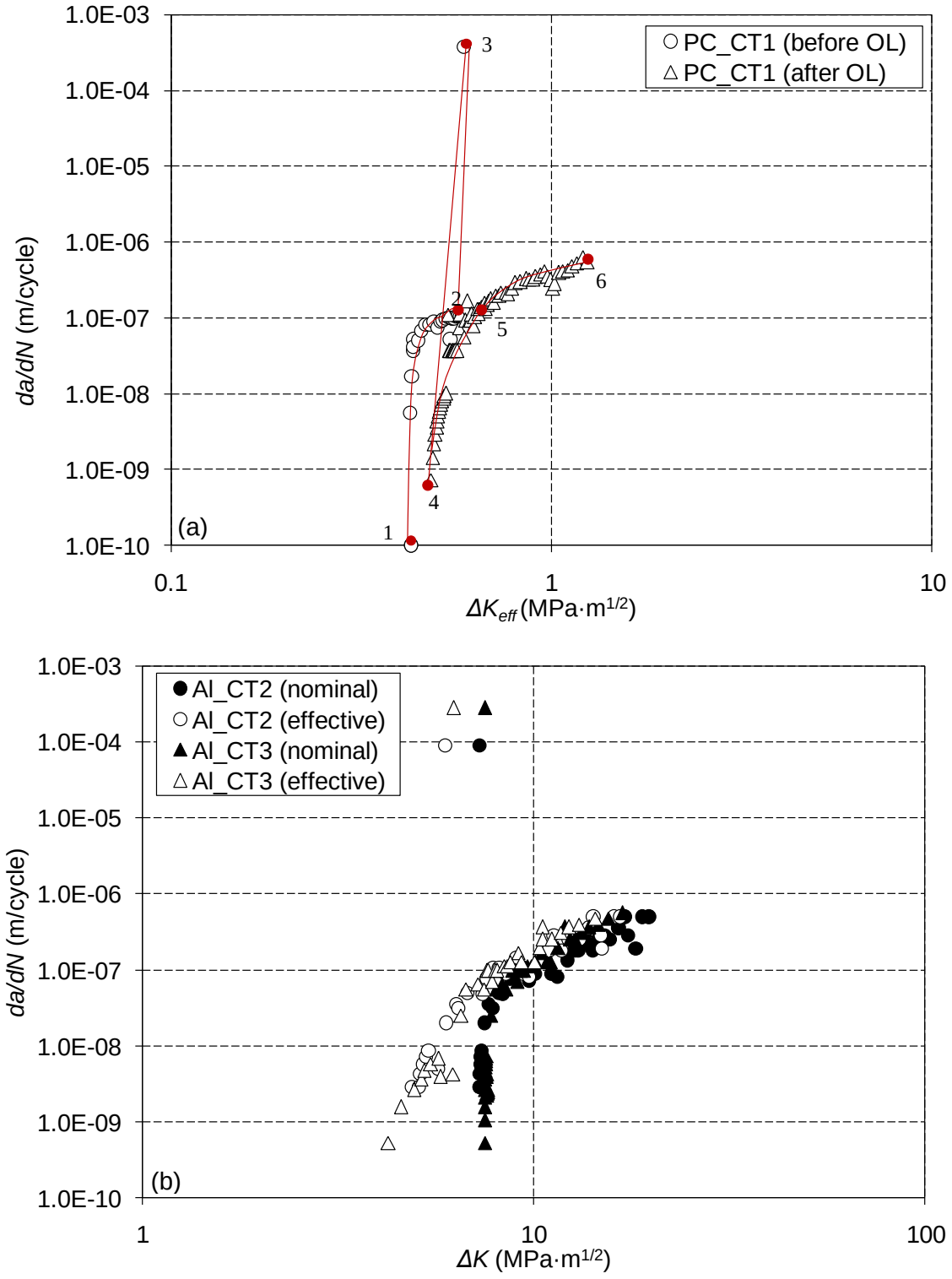

Figure 13 (a) Typical *da/dN* vs ΔK_{eff} data through a 200% overload for the polycarbonate specimen; (b) *da/dN* vs ΔK_{nom} and ΔK_{eff} for the aluminium specimens.

Cycle immediately prior to the overload

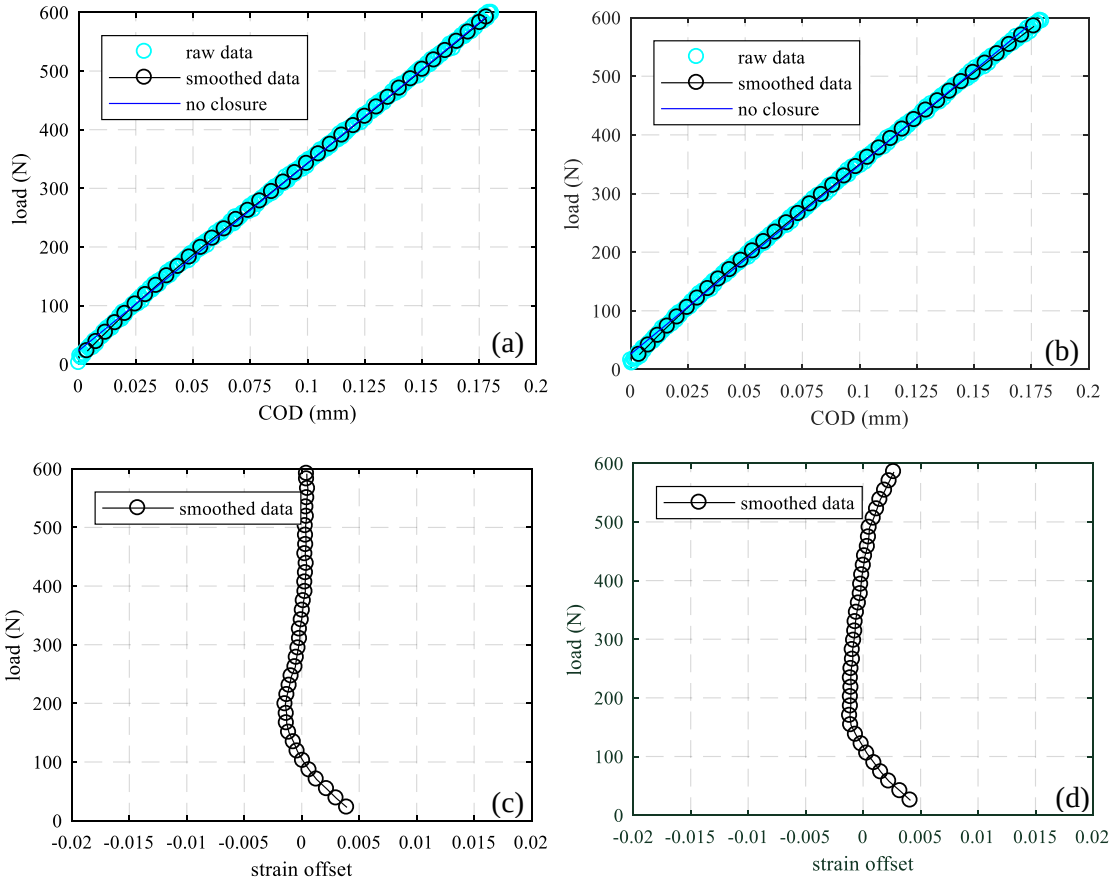

Cycle immediately after the applied overload

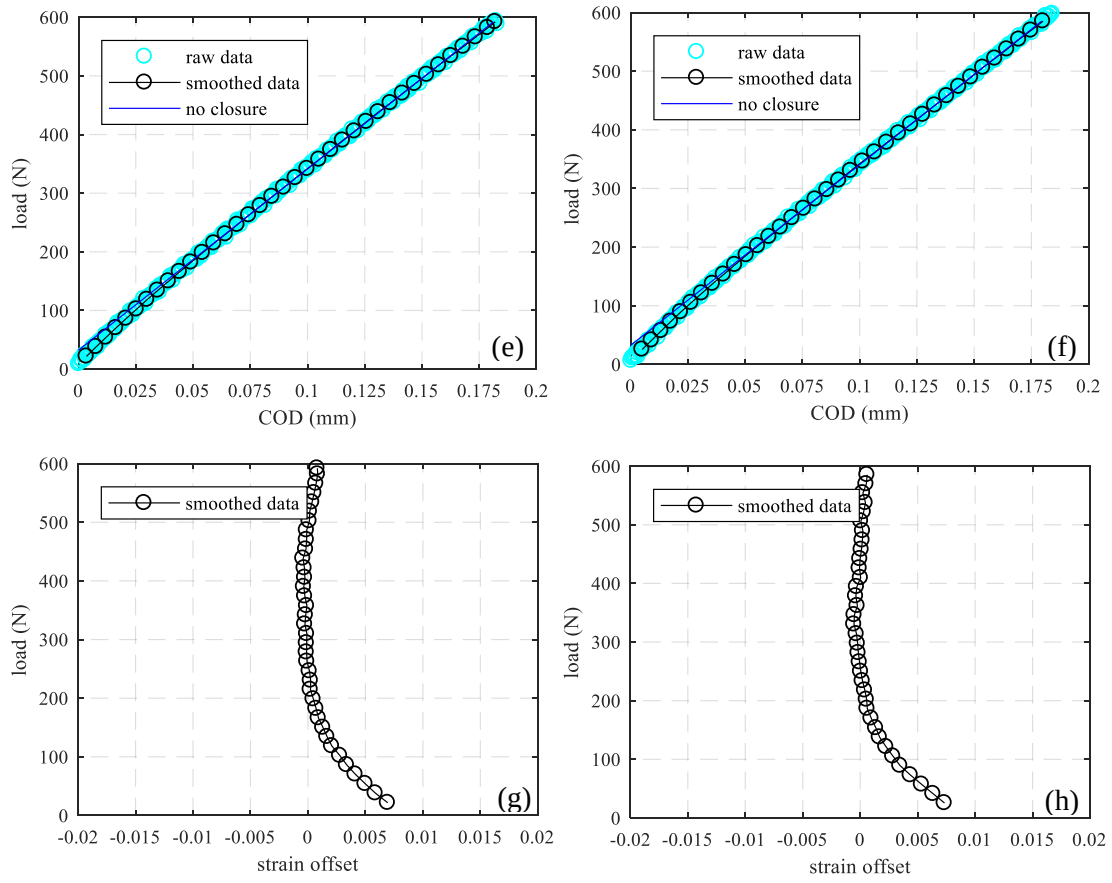

Figure 14 Compliance data for the AL_CT3 specimen corresponding with the load cycles immediately prior to, and immediately after, the 125% overload: (a) and (e) load (*P)* vs crack opening displacement (COD) for the loading half cycle; (b) and (f) *P* vs COD for the unloading half cycle; (c) and (g) *P* vs offset strain for the loading half cycle; (d) and (h) *P* vs offset strain for the unloading half cycle.

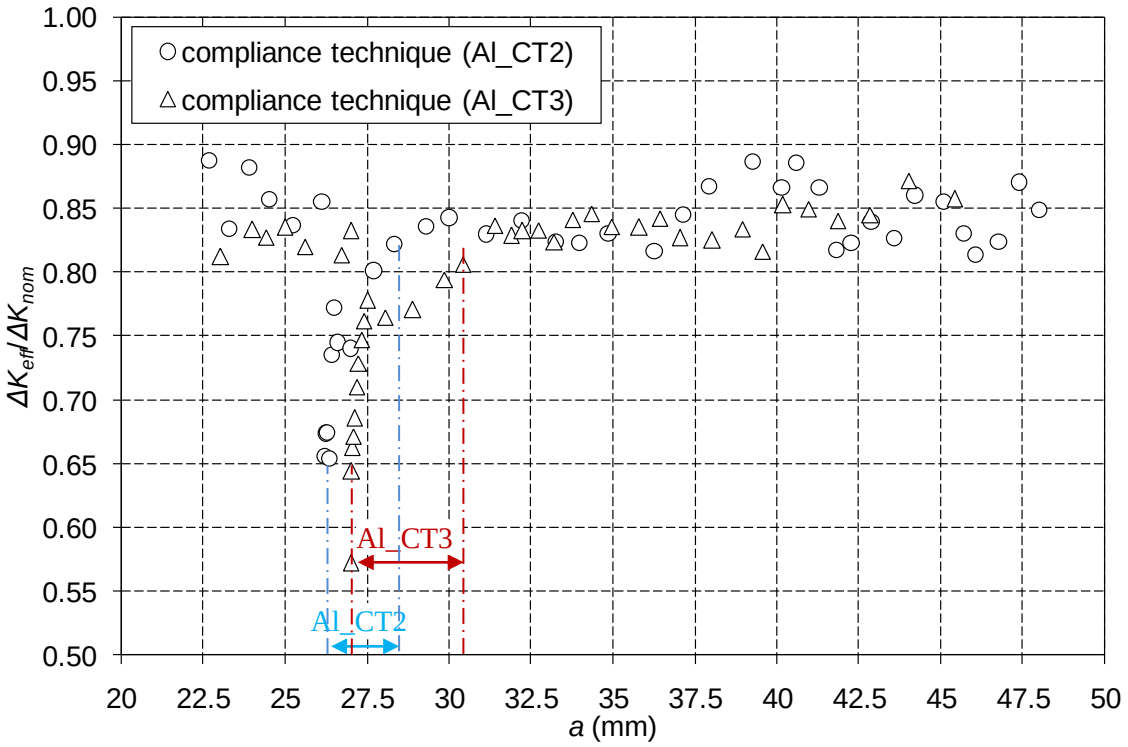

Figure 15 Variation in the ratio $\Delta K_{eff}/\Delta K_{nom}$ (measured using the offset compliance technique) with crack length before and after the 125% overload for the AL3_CT specimen.

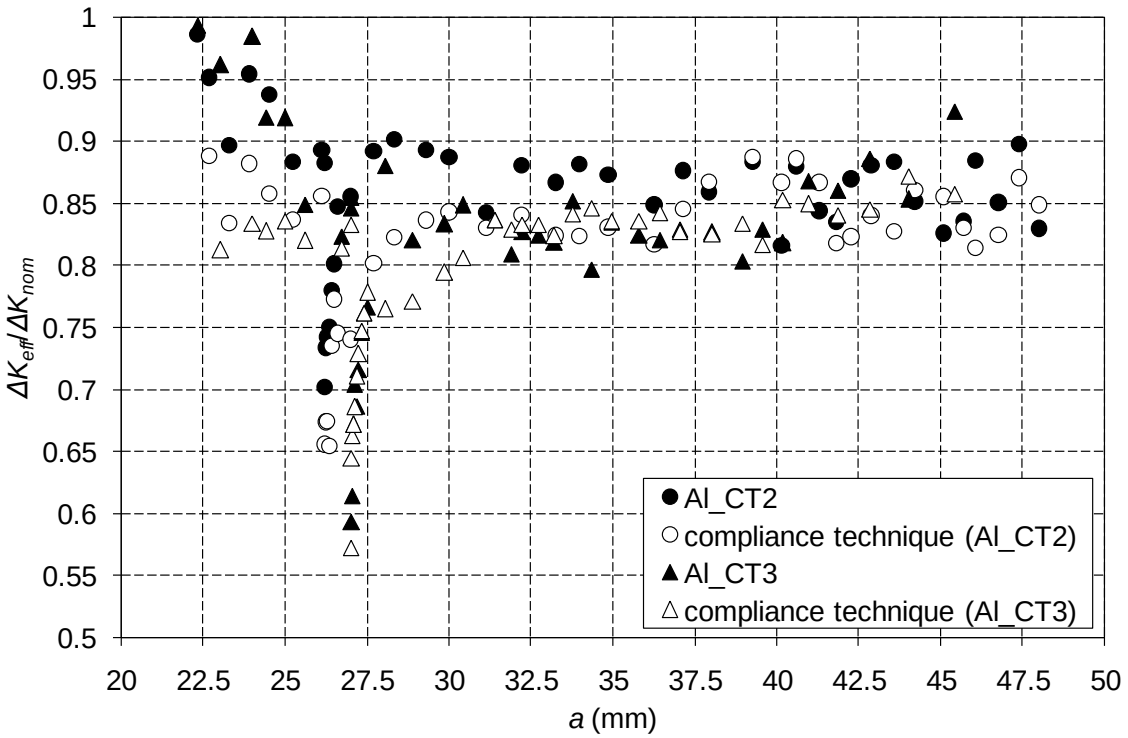

Figure 16 Comparison between the ratio $\Delta K_{eff}/\Delta K_{nom}$ as a function of crack length for the aluminium specimens obtained using the CJP model and using the offset compliance technique.

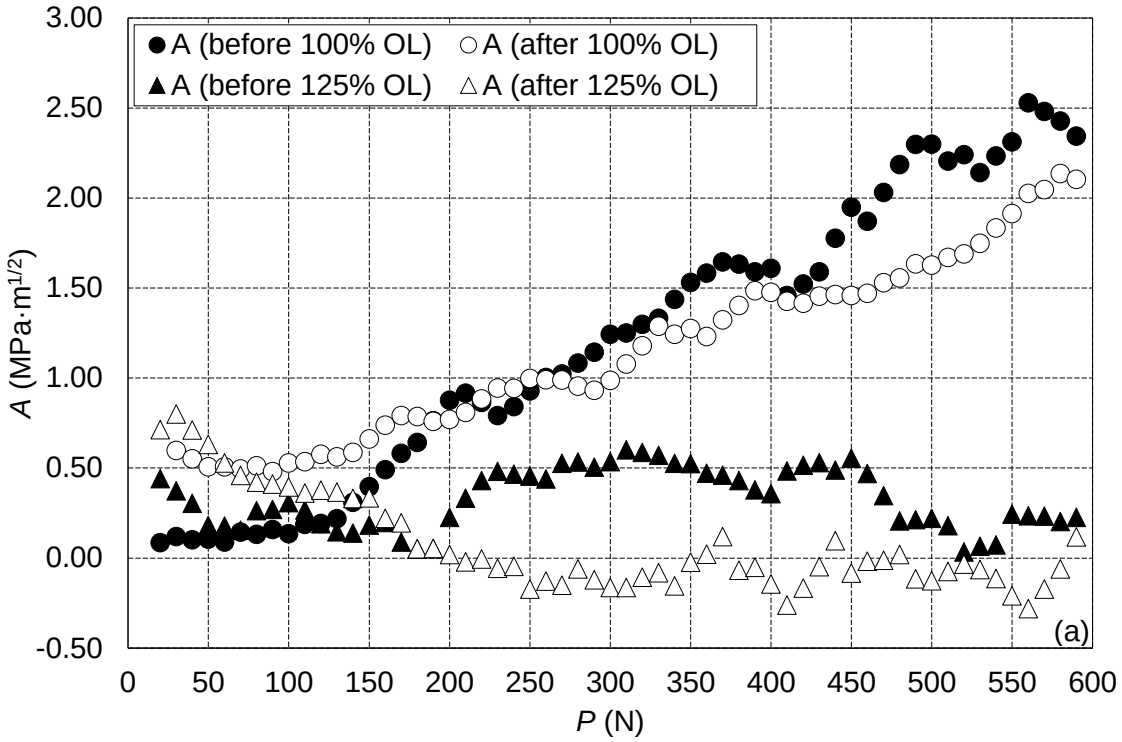
A (before 100% OL)
A (after 100% OL)
A (before 125% OL)
A (after 125% OL)
A (MPa·m^1/2)
P (N)
(a)

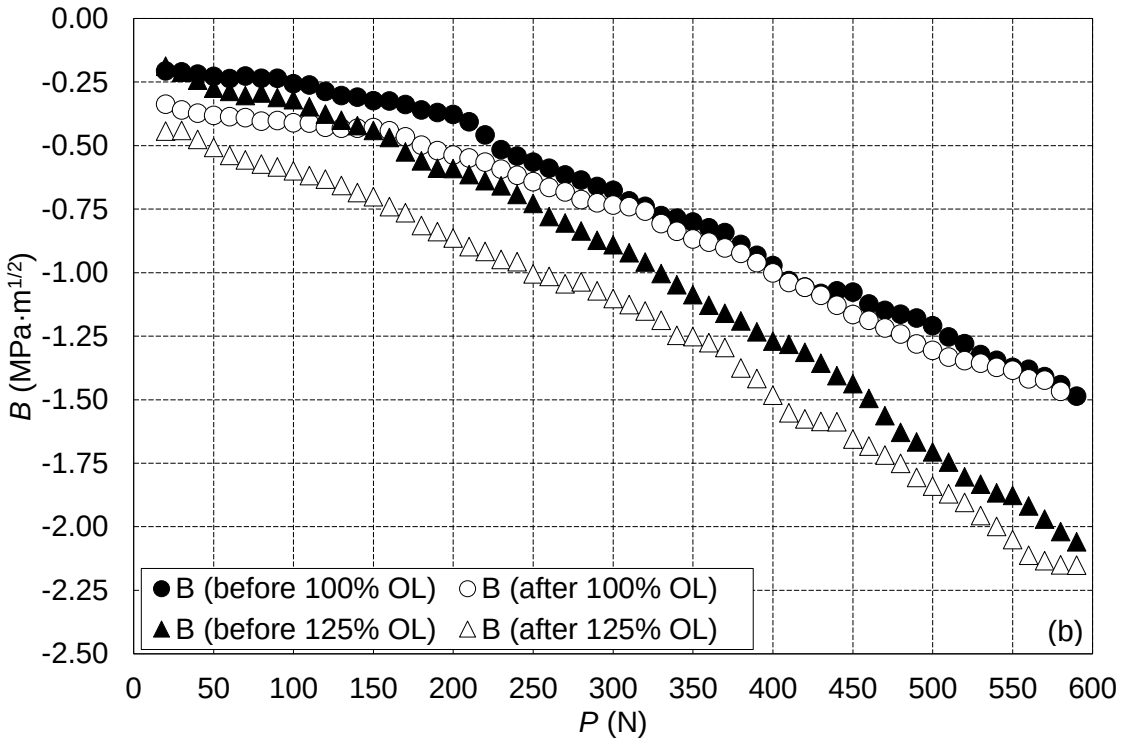
B (before 100% OL)
B (after 100% OL)
B (before 125% OL)
B (after 125% OL)
B (MPa·m^1/2)
P (N)
(b)

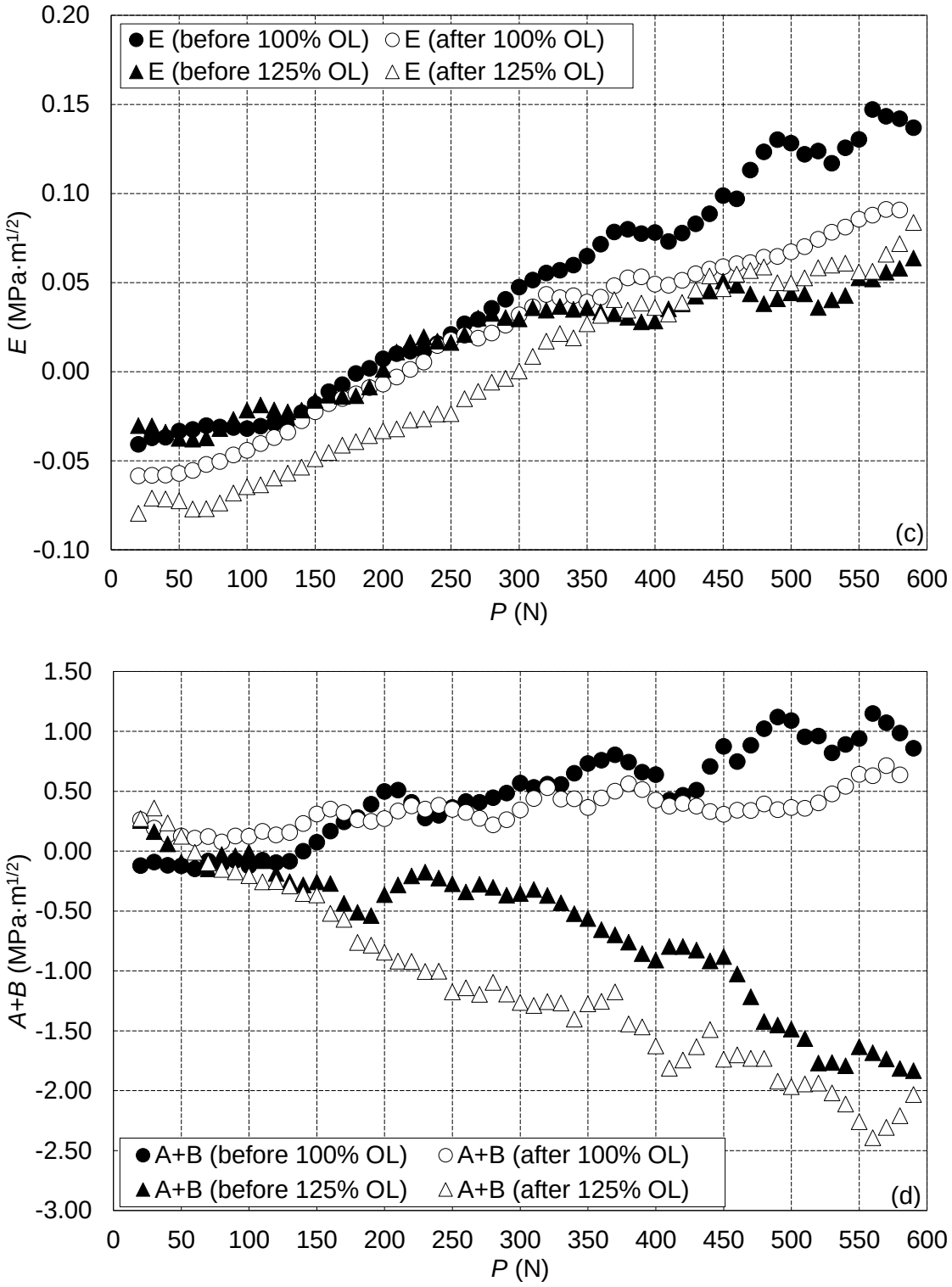

Figure 17 Changes in the parameters through a loading half cycle following an overload: (a) *A*, (b) *B*, (c) *E* and (d) *A*+*B*.